TOPICAL REVIEW

Energy dispersive x-ray reflectometry as a unique laboratory tool for investigating morphological properties of layered systems and devices

V Rossi Albertini, B Paci and A Generosi

Istituto di Struttura della Materia, C.N.R., Via del Fosso del Cavaliere 100, 00133 Roma, Italy

E-mail: valerio.rossi@ism.cnr.it, barbara.paci@ism.cnr.it and amanda.generosi@ism.cnr.it

Abstract
The principles and technical aspects of the laboratory energy dispersive x-ray reflectometry technique (EDXR) are reviewed. X-ray reflectometry enables us to retrieve information on the morphological parameters (film thickness, surface and interface roughness) of thin films, layered materials and devices at the Å resolution. In the energy dispersive mode it makes use of a polychromatic beam and the energy scan is carried out by means of an energy sensitive detector, allowing us to keep the experimental geometry unchanged during data collection. The advantages offered by the technique, in particular when accurate time-resolved studies are to be performed, are outlined. An overview of the most significant works in the field is also reported, in order to present the wide range of its possible applications. The paper was written taking into account the necessity to provide a comprehensive description of this unusual laboratory technique. The first part of the manuscript is, therefore, devoted to the general aspects of EDXR: theoretical bases, experimental characteristics, advantages and drawbacks in comparison with alternative techniques, instrumental effects that may occur and information that can be gained by its application. In the second part of the paper, we resume the main literature results obtained by applying it to a variety of systems, to show examples of the possibilities it offers. Among the experiments reported, in particular much emphasis is given to the time-resolved *in situ* ones (for example, devices upon working and systems undergoing morphological modifications), which probably represents the most original use of this method.

(Some figures in this article are in colour only in the electronic version)

1. Introduction

Since the first experiments carried out in 1954 [1], x-ray reflectivity (XR) has proved to be a powerful tool for investigations on layered media [2–6]. Subsequently, it has been applied in many different contexts [7–14], both alone and together with other experimental techniques [15–18], for a more complete characterization of the sample's properties.

An XR experiment traditionally consists of measuring the intensity of the incident monochromatic x-ray beam reflected by the sample as a function of the reflection angle, at and above the critical reflection threshold. Therefore, regardless

of whether the incident x-ray beam is generated by a laboratory x-ray tube or a large scale source, such as a synchrotron [19], the working principle is an angular scan in the vicinity of the critical edge. However, much like x-ray diffraction, the parameter on which the reflected intensity (and, therefore, the position of the critical edge) depends is the momentum transferred from the incident radiation to the sample atoms, as will be shown in the following section [20–24]. Since, in turn, the momentum transfer is a function of both the reflection angle and the x-ray energy, two ways are available for collecting a reflection pattern. The first is the traditional mode, which consists of measuring the reflected intensity as a function of the angle, keeping the x-ray energy unchanged [25–28]; the second, conversely, consists of measuring the reflected intensity as a function of the x-ray energy, keeping the reflection angle unchanged. The first possibility takes the name angular dispersive (AD) technique; the second, energy dispersive (ED) technique [29, 30]. In AD, a monochromatic radiation must be used and the angular scan is carried out either mechanically or by means of a spatially extended detector such as, for instance, an image plate. In ED, instead, a polychromatic x-ray beam (which is often referred to as a 'white beam', in analogy with visible radiation) must be utilized and the scan is executed electronically by a solid state detector (SSD). From this point of view, the differences between AD x-ray reflection (ADXR) and ED x-ray reflection (EDXR) are similar to those between their diffraction counterparts, which are more widely known and utilized. It is evident that, using ED, the experimenter must deal with the problems involved by the simultaneous presence of photons having different energies, which interact in different ways with the sample material. Indeed, x-ray reflection is accompanied by a number of concomitant energy-dependent effects due to both the sample (x-ray absorption and the emitted fluorescence lines) and the instrumental components (the transparency of the collimating slits, the resolution of the detector, etc). Nevertheless, the fixed geometry of the ED x-ray machines can represent an extraordinary advantage in many cases of interest. Other advantages and drawbacks of the two techniques will be mentioned in section 3, where the ED approach to XR is discussed.

In the following, attention will be focused on laboratory EDXR, since the aim is to show how a simple x-ray machine [31], which can be obtained by slightly modifying an ED x-ray diffractometer to allow grazing incidences of the x-ray beam, can be a very useful tool in the study of stratified media. Our experience in the field is that an ED x-ray machine is able to carry out both diffraction and reflection measurements easily, by applying just a few precautions to prevent problems and artefacts, that are otherwise likely to occur.

Section 4 will contain examples of the application of the EDXR reported in the literature to measure samples electron density [32]. In section 5, papers concerning the use of EDXR to obtain morphological information will be reviewed [33–43]. Finally in section 6, a particular aspect of the laboratory EDXR technique, time-resolved *in situ* investigations to observe the modifications occurring in stratified systems undergoing morphological changes, will be examined in depth [44–51]. To this category belong, for instance, oxide films growing on clean (solid or liquid) surfaces, organic films submitted to thermal treatments (annealing), films deposited on substrates by thermal or electron beam evaporations and ion beam sputtering, organic solar cells upon illumination and sensing films exposed to gases or water vapours. Indeed, EDXR measurements are extremely suitable for these kinds of *in situ* studies because of the above-mentioned static geometry of the setup in which the measurement is performed.

The scope of this paper is, therefore, to provide a general overview of the EDXR technique, to report works carried out relating to it and, finally, to give practical suggestions to the researcher who might be interested in trying it.

The theory of x-ray reflectometry will be discussed in the next section, providing a brief outline which will serve as an introduction for the reader who may not be familiar with the subject. However, rigorous and deep treatments, which may be found in books and papers cited there and throughout the text, will be avoided since they are beyond the purpose of this review.

2. Elements of x-ray reflection theory

While a great deal of work has been dedicated both to the theory of the XR and to the general features of the experimental XR technique, almost always identified with its angular dispersive mode, no comprehensive treatment of the laboratory EDXR has been attempted till now.

Therefore, instead of repeating in the present section an extensive discussion on these subjects, which can be found reported in several textbooks [52, 53], we shall summarize the XR theory in reference with its application to the ED case, following the excellent review by Zhou and Chen [54].

Usually the x-ray diffraction theory is developed making use of the classical electromagnetism, rather than of the exact quantum theory [55, 56]. This approximation works well as long as the elastic x-ray scattering is concerned. However, when the momentum transfer is raised, a progressively increasing fraction of the x-ray radiation begins to be scattered inelastically. Such inelastic contribution cannot be obtained from the classical theory and must be introduced ad hoc, for instance by adding an extra term (usually derived by the semi-classical Compton model) in the scattering equation. The same should apply to x-ray reflection but, since the refractive index of matter in this energy range is very close to unity [57,58], the scattering (reflection) angle is extremely small, as well as the momentum transfer. As a consequence, no significant error is committed if Maxwell's equations are used to describe the phenomenon.

The starting problem is to calculate such a refraction index. This can be done by considering the oscillations of the bound atomic electrons induced by the x-rays electric field when the medium is irradiated. Newton's law for such electrons contains three terms: the electric force (F_e), proportional to both the electric field and the electron charge; a restoring force (F_R), due to the binding of the electrons with their nuclei, which can be modelled as a Hooke's contribution proportional to the electron displacement; a dissipative force (F_D), due to re-irradiation of the oscillating charges. The latter term cannot be written directly. It is derived by the equation expressing the average power loss over a whole cycle of the

electron as a function of the second derivative of the dipole moment associated with the electron itself [54]. Therefore, $m_e a = F_e + F_R + F_D$, where m_e and a are the electron mass and acceleration.

The solution of the so obtained Newton's equation correlates the polarization density P of the medium with the radiation electric field E at the position r:

$$P(r) = -\frac{\varepsilon_0 \lambda^2}{\pi} \rho(r) E(r),$$

$$\rho(r) = \frac{r_0 N(r)}{1 - (\lambda/\lambda_i)^2 + i4\pi r_0/3\lambda},$$

where ε_0 is the dielectric permittivity of the vacuum, λ and λ_i are the wavelength and the resonance wavelength, respectively, ρ is called the (complex) scattering length density, r_0 is the classical electron radius and N is the number electron density.

These expressions can be used to close the relation obtainable from the two Maxwell's equations that involve the curls of the electric and magnetic field of a monochromatic radiation in the medium:

$$\nabla \times \nabla \times E(r) - k_0^2 E(r) = -4\pi \rho(r) E(r), \quad (2.1)$$

where k_0 is the free-space three-dimensional wavenumber of the radiation.

The equation can be rewritten as

$$\nabla \times \nabla \times E(r) - k_1^2(r) \cdot E(r) = 0, \quad (2.2)$$

where $k_1(r) = \sqrt{k_0^2 - 4\pi\rho(r)}$.

By the usual definition of the refractive index as the ratio between the wavenumber in the medium and the wavenumber in the free space, $n(r) = (k_1(r)/k_0)$.

Since $k_0 = 2\pi\lambda$ and the variation of the wavenumber when the x-rays enter the medium is small, at the first approximation in ρ, n results in

$$n \cong 1 - \lambda^2 \rho/2\pi.$$

By substituting the previous expression of ρ, this relation is usually written as

$$n \cong 1 - \delta - i\beta,$$

where δ and β are related to the real (ρ') and imaginary (ρ'') parts of ρ through

$$\delta = (\lambda^2/2\pi)\rho',$$
$$\beta = (\lambda^2/2\pi)\rho''.$$

The x-ray absorption is due to the latter term. Indeed, it generates an exponential coefficient in the equation of the wave propagation in a medium that decreases the wave amplitude.

The form factor, or scattering amplitude f, defined as the ratio between the amplitude of the radiation scattered by the electrons contained in a certain volume of the medium and the amplitude of the radiation scattered by the same number of free electrons, is therefore in close connection with the scattering length density:

$$f = f_0 + \Delta f' + i\Delta f'' = \frac{\rho}{r_0 N},$$

and so $\rho' = r_0 N(f_0 + \Delta f'')$ and $\rho'' = r_0 N \Delta f''$.

As a consequence, since at very small momentum transfers the normal scattering amplitude f_0 tends to the atomic number Z,

$$\delta = r_0(N_A/2\pi)(Z + \Delta f')\lambda^2$$

and

$$\beta = r_0(N_A/2\pi)\Delta f''\lambda^2,$$

where N_A is the number of atoms per unit volume and $(\Delta f', \Delta f'')$ are the anomalous scattering corrections, whose values are small compared with Z except close to the absorption edges.

In the case of a homogeneous medium, assuming the direction perpendicular to its surface as the z axis, the electric field E is invariant in the xy plane. The z component of E at the two sides of the vacuum–medium interface can be attained by using equation (2.1), together with its counterpart in the vacuum ($\rho = 0$):

$$\frac{dE_z^2(z)}{dz^2} + k_{0z}^2 E_z(z) = 0 \qquad z < 0 \text{ (in the vacuum)},$$

$$\frac{dE_z^2(z)}{dz^2} + k_{1z}^2 E_z(z) = 0 \qquad z > 0 \text{ (in the medium)}. \quad (2.3)$$

with $k_{1z} = k_{0z} \sin\vartheta = \sqrt{k_{0z}^2 - 4\pi\rho}$.

It can be noted that k_{1z} is always smaller than k_{0z}. On the other hand, k_{1z} becomes imaginary as soon as $k_{0z}\langle 4\pi\rho$. The threshold value for k_{0z}, at which $k_{1z} = 0$, takes the name of *critical point of total reflection*

$$k_c = \sqrt{4\pi\rho}. \quad (2.4)$$

A solution of Helmholtz equations (2.3) for an incident wave of unitary amplitude is

$$U(z) = e^{ik_{0z}z} + Re^{-ik_{0z}z} \qquad \text{for } z < 0 \text{ (in the vacuum)},$$

$$U(z) = Te^{ik_{0z}z} \qquad \text{for } z > 0 \text{ (in the medium)}.$$

Actually, the two equations (2.3) apply rigorously in the case of s-polarized (perpendicular to the incidence plane) electromagnetic waves only. However, due to the small value of ρ, the equations are also correct for p-polarized waves (parallel to the incidence plane) at a very good approximation.

The reflected (R) and transmitted (T) amplitudes, called Fresnel reflectance and transmittance, respectively, are to be determined. This can be done by imposing the continuity condition of the electric field and of its first derivative at the interface ($z = 0$): $1 + R = T$ and $k_{0z}(1 - R) = k_{1z}$:

$$R = \frac{k_{0z} - k_{1z}}{k_{0z} + k_{1z}},$$

$$T = \frac{2k_{0z}}{k_{0z} + k_{1z}}.$$

Below the critical point, $|R|^2$, called the Fresnel reflectivity, is equal to unit (total reflection plateau). Above the critical point, $|R|^2 < 1$ (partial reflection condition).

Adopting the diffraction formalism, the reflectance can be written in terms of the z-component of the momentum transfer
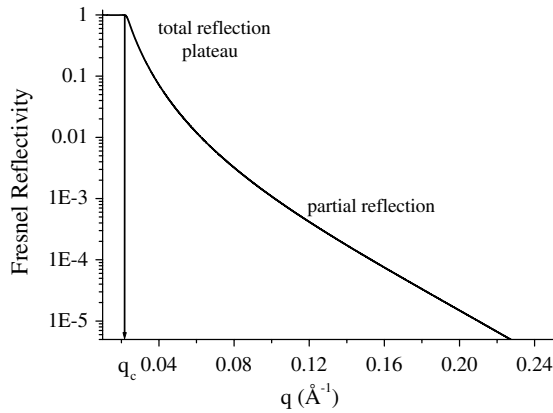
Figure 1. Fresnel reflectivity of a blank surface with no absorption from which the critical scattering parameter q_c can be deduced.

q_z and of its critical value q_c, taking into account that, in specular conditions, q_z is twice the k_{0z} component:

$$R = \frac{q_z - \sqrt{q_z^2 - q_c^2}}{q_z + \sqrt{q_z^2 - q_c^2}}, \qquad \text{where } q_c = 4\sqrt{\pi\rho}.$$

At large q values, the right-hand side of this equation can be expanded in powers of ρ at the first order. Therefore, $R \approx 4\pi\rho/q_z^2$ and $|R|^2 \approx (4\pi|\rho|)^2/q_z^4$. The latter is referred to as the Porod's q^{-4} law.

The effect of the imaginary part of ρ is a decrease in the reflected wave amplitude (x-ray absorption) and a consequent modification of the reflection pattern profile. Since the penetration depth for q below q_c is very small, the total reflection plateau is almost unaffected by absorption (figure 1). However, as soon as the radiation starts to penetrate the medium (for $q > q_c$), the absorption becomes relevant and produces a rounding of the sharp total reflection edge.

In the case of a stratified sample, having more than one interface (see figure 2), the previous equation must be extended.

The formalism to describe this case is due to Parratt [1], who developed a recursive formula based on the reflectance $R_{j,j+1}$ at the jth interface (namely, between layer jth and layer jth + 1) [36]:

$$R_{j,j+1} = \frac{q_{z,j} - q_{z,j+1}}{q_{z,j} + q_{z,j+1}} \qquad \text{where } q_{z,j} = \sqrt{q_z^2 - q_{c,j}^2}.$$

(2.5)

The Parratt's formula expresses the reflectance r_j of the entire region beneath the interface jth (that is to say between the jth layer and the substrate) in terms of the overall reflectance r_{j+1} beneath the interface jth + 1 and of the single interface reflectance $R_{j,j+1}$:

$$r_j = \frac{R_{j,j+1} + r_{j+1}e^{iq_{z,j+1}\Delta z_{j+1}}}{1 + R_{j,j+1}r_{j+1}e^{iq_{z,j+1}\Delta z_{j+1}}}, \qquad (2.6)$$

where Δz_{j+1} is the thickness of layer jth + 1.

An alternative approach leading to the same results is based on the matrix formalism. It represents the reflection inside the layered systems by means of a couple of matrices for each layer, which describe the behaviour of the radiation electric field in the layer [59, 60].
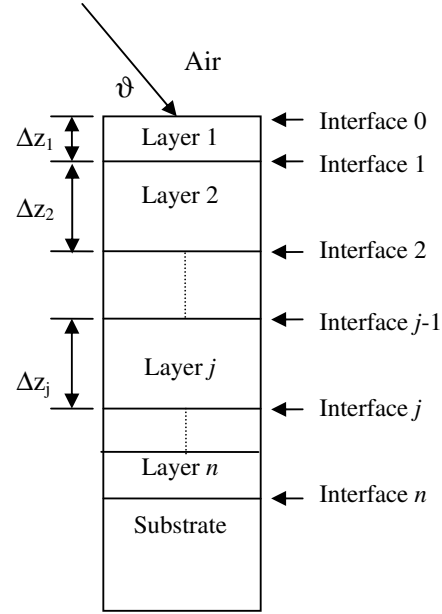
Figure 2. A schematic diagram showing the definitions used in the Parratt formalism for a multilayered film.

The waves partially reflected at the interfaces between adjacent layers interfere producing modulations, referred to as Kiessig fringes [61], in the overall reflected signal. The frequencies of the modulations bring the information on the thicknesses of the layers and on their periodicity.

A particularly interesting case is when $j = 2$, which represents the model of a film deposited on a semi-infinite substrate. For a film of thickness d, defining as R_s, R_i and R_{tot} the film surface, the film–substrate interface and the overall system reflectances, respectively, the previous formula can be rewritten as

$$R_{tot} = \frac{R_s + R_i e^{iq_{z,1}d}}{1 + R_s R_i e^{iq_{z,1}d}}$$

and the reflectivity

$$|R_{tot}|^2 = \frac{R_s^2 + R_i^2 + 2\,R_s R_i \cos(q_{z,1}d)}{1 + R_s^2\,R_i^2\,\cos(q_{z,1}d)}.$$

At large q values, $q_{z,j}$ approaches q_z (see equation 2.5) and the reflectivity becomes

$$|R_{tot}|^2 = \frac{16\pi^2}{q_z^4}[\rho_{film}^2 + (\rho_{sub} - \rho_{film})^2$$
$$+ 2\rho_{film}(\rho_{sub} - \rho_{film})\cos(q_zd)].$$

Therefore $|R_{tot}|^2$ is an oscillating function of period $2\pi/d$, decreasing as q_z^{-4}, according to Porod's law.

From the oscillation period at high q_z, the film thickness can be obtained directly: $d = 2\pi/\Delta q_z$, where Δq_z is the q-distance between two adjacent peaks.

To account for the non-ideal flatness of real surfaces and interfaces [62], terms related to their roughness have to be included in the Parratt equation as damping coefficients of the oscillating components. The two most used expressions for these coefficients are the Debye–Waller and the Nevot–Croce [63, 64] factors. The former is analogous to that used in diffraction to take into account the thermal motions of the
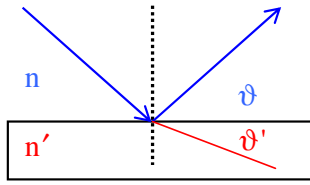
Figure 3. Schematic sketch of the interaction of an x-ray beam upon a surface.

particles around their equilibrium positions. The latter is similar to the other, but the square of the radiation wave number in the medium of provenance is replaced with the product of the wave numbers in the two media separated by the interface. The effect of the roughness is to diffuse the incident radiation off the specular direction.

Other models and approximations could be cited but, since they were not used in any of the papers discussed in this review, they will not be reported here. The interested reader is addressed to [65, 66].

3. Outline of energy dispersive x-ray reflectivity

3.1. Comparison of the ED mode with the AD one: advantages and drawbacks

As mentioned, in x-ray diffraction, the energy dispersive mode (EDXD) is usually introduced in comparison with its angular dispersive counterpart (ADXD) [67]. This guarantees an easier understanding of the characteristics, drawbacks and advantages of EDXD, owing to the universal knowledge of the traditional AD technique.

For energy dispersive x-ray reflection, the same approach will be taken, since it allows us to refer to the vast literature on the angular dispersive one, avoiding unnecessary repetitions.

The alternative AD/ED is a common feature of all those scanning techniques that consist of collecting, as a function of momentum transfer, the intensity of an x-ray beam after it has interacted with the sample. Techniques having this characteristic are those based on the scattering of x-ray radiation by the sample electrons. Diffraction (interference of elastically scattered x-rays) inelastic compton scattering, small angle scattering, reflection (again a collective effect of the x-rays scattered by each point of the surface) are all examples of these techniques.

Momentum transfer is often normalized to the speed of light and to Planck's constant. In this case, it takes the name *scattering vector $\mathbf{q}$* and its amplitude *scattering parameter q*.

The *scattering parameter* depends on both the deflection angle and the x-ray energy. In the case of x-ray reflection, this can be shown in a more direct and simple manner equivalent to that discussed in section 2, making use of Snell's law applied to this energy range: $n \cos \vartheta = n' \cos \vartheta'$. Snell's law describes the relation between the incidence and the refraction angles (ϑ and ϑ') of an x-ray beam at the interface between two materials of different refraction indices (n, n'), as shown in figure 3.

The critical angle for total external reflection ϑ_c is defined as the angle below which the x-ray radiation does not penetrate the second medium anymore (apart from a stationary exponentially decreasing tail) and is totally reflected. Therefore, in total reflection conditions (below ϑ_c)
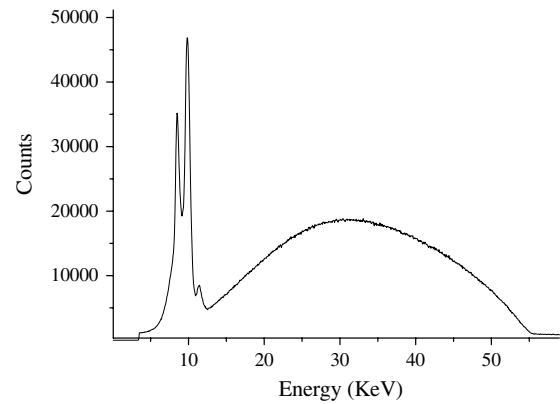
Figure 4. The continuous Bremmsstrahlung component of the W tube radiation (white beam) is plotted as a function of its energy (0–55 keV). The sharp peaks in the 8–13 keV range are the Tungsten L fluorescence lines.

from the surface of a medium in the vacuum (or air), $n = 1$, $\vartheta' = 0$ and $\cos \vartheta = n'$. In the x-ray energy range, the refractive index n' can be expressed as reported in equation (2.2).

At grazing angles, the expansion of the cos-function at the second order is a very good approximation, so that Snell's law becomes $\cos \vartheta_c \cong 1 - (1/2)\vartheta_c^2 = 1 - (N\lambda^2 r_0)/2\pi$; $\vartheta_c^2 = (N\lambda^2 r_0)/\pi$.

Since the scattering parameter is defined as

$$q = 4\pi \sin \vartheta/\lambda = aE \sin \vartheta, \qquad \text{where } a = \frac{2}{\hbar c} \qquad (3.1)$$

and $(\vartheta_c/\lambda) = \sqrt{r_0 N/\pi}$, in the same approximation of grazing angles as before, the critical conditions are approached when $q = q_c \cong \sqrt{\pi r_0 N} = \text{const}$.

Therefore, scanning the reciprocal space is the natural way to collect a reflection pattern, such as for diffraction. According to equation (3.1), this can be done either by scanning the angle while the energy is kept unchanged (conventional angular dispersive mode) or, reversely, by scanning the energy at a fixed angle (energy dispersive mode).

When the experiment is carried out in AD mode by using a laboratory x-ray tube source, the monochromatic beam is obtained by selecting a fluorescence line. The scan is generally carried out in a mechanical way, by progressively rotating the two x-ray machine arms on which the tube and the detector are mounted, respectively.

In the case of ED, instead, no movement is required. The x-ray beam is polychromatic, typically the continuous Bremmsstrahlung (braking radiation) component of the tube radiation, and the scan is executed electronically by an energy dispersive solid state detector. From this point of view, the ED mode can be considered a spectroscopic way of performing scattering experiments.

An example of the primary x-ray beam used for EDXR experiments is shown in figure 4.

It is formed by two components: a discrete part represented by a series of fluorescence lines of the tube target (in this case, tungsten L lines) and a continuous component corresponding to Bremmsstrahlung. Tungsten is to be preferred to other more common x-ray tube anodic materials, such as Cu or Mo, because the Bremmsstrahlung intensity emitted by tubes

is an increasing function of the density of the material. Its spectrum ranges from zero (the softer components being strongly attenuated by the tube and detector Be windows) to a maximum value depending on the x-ray power supply voltage. Indeed, by definition, if the applied voltage is n kV and the initial kinetic energy of the electrons accelerated by this voltage is negligible, the final energy value is n keV. Since the maximum energy E_{max} of the breaking radiation equals that of the electrons (in the case the electrons being completely stopped in a single event and hence transferring their energy totally to the photon produced), its spectrum ranges from zero to n keV.

Alternatively, in experiments performed at synchrotron facilities, the radiation emitted by bending magnets was utilized for the same purpose. In particular, at the storage ring Bessy I [68] and, subsequently, at Bessy II (Berlin, Germany) [69], an EDXR facility was installed, which makes use of a primary beam characterized by an exponentially intensity decay in the range $3\,keV < E < 35\,keV$. The high integrated intensity allows shorter collection times, although some problems may arise because of the remarkable intensity variation along the spectral profile. Indeed, since the photon flux varies over five orders of magnitude in the energy region of interest, absorber foils of different thicknesses must be interposed to balance such a difference and to prevent detector saturation [70].

ED x-ray diffraction dates back to 1968 when Giessen and Gordon [71] reported the first measurement of this kind. However, fourteen years passed before the first ED x-ray reflection experiment was carried out by Bilderback and Hubbard [33, 34]. The reason for this delay was probably the scarcity of information regarding this new development and the overestimation of its supposed drawbacks.

The ED mode contains, in fact, an intrinsic limit that may compromise the result of high resolution measurements. In AD, the only contribution to the uncertainty on the scattering parameter comes from the angular spread, the x-ray energy spread (due to the natural width of the fluorescence line) generally being negligible. Hence, in an ideal case, an arbitrarily high angular resolution could be reached by reducing the aperture of the slits, although at the cost of a consequent decrease in the photon flux at the detector. Instead, in ED, the finite energy resolution of the detector must also be taken into account [72]. To show this in quantitative terms, the logarithmic derivative of both sides of equation (3.1) can be calculated:

$$\frac{\Delta q}{q} \cong \frac{\Delta E}{E} + \mathrm{ctg}\vartheta \, \Delta\vartheta. \qquad (3.2)$$

The first term on the right-hand side represents a lower limit to the relative q-resolution in ED.

Although this limit may be a serious difficulty in many x-ray diffractometry studies, the problem is not so severe in reflectivity studies. Indeed, a typical reflectivity pattern is characterized either by long period oscillations (films and multilayers) or by broad Bragg-like peaks (superlattices). This is due to the fact that the q-interval $q_c \leqslant q \leqslant q_{max}$, above which q_{max} the (partially) reflected intensity gets too low to be detected, corresponds, 'in direct space', to a few hundreds nanometres. In such a d-range, typical superlattices may contain a few periods only (otherwise diffraction is the suitable

technique to study these samples), and the interference of the waves reflected at the interfaces between adjacent stacks does not produce strong modulations. As a consequence, further broadening of the reflection signal due to its convolution with the instrumental transfer function is expected to have, in most cases, only minor effects or, at worst, effects that do not compromise the result of the measurement. A simple instance of the latter case is the study of a thin film deposited on a substrate. The high q tail of the reflection curve, according to that discussed in section 2, is represented by a damped (because of the Porod's decay and of the roughness factor) oscillating intensity. The oscillation is the modulus of a co-sinusoidal (section 2) function and has sharp cuspidal minima. If such cuspids are rounded as an effect of the poor resolution, the fitting procedure making use of the function in equation (2.6) interprets the round shape as a lower optical contrast between film and substrate. In this case, a constraint based on prior information on the densities must be imposed. Another case where high resolution would be required to observe high frequency oscillations, which otherwise are washed out, can be found in [47]. A comparison between an ADXR and an EDXR measurement can be found in [68], where the same sample (a stack of 12 monolayers of Mg stearate) was studied using both techniques. Apart from a little difference in the resolution, the reflectivity patterns are practically equivalent.

A second drawback, which has a smaller impact in EDXR than in EDXD, is the limited accessible range in the q space at a fixed deflection angle. According to equation (3.1), at a given angle ϑ and for a given maximum energy E_{max}, this range should span from zero to a $q_{max} = aE_{max}\sin\vartheta$

From this point of view, a change in ϑ, which acts as an instrumental parameter to be set before the beginning of the measurement, corresponds to an expansion or contraction of the accessible window in the reciprocal space. Theoretically, therefore, just a single measurement at the highest possible angle would be required, because any other measurement at a smaller angle would produce a pattern contained in a narrower q interval, not providing further information on the system. Unfortunately, not all the energy spectrum can actually be utilized, for the lowest and the highest energy parts have an intensity which is too weak (see figure 4). Hence, to cover the q-interval of interest, several patterns must be collected in correspondence to a set of angular values [67]. Alternatively, the use of a multi-element detector, in a linear array configuration, was suggested [73].

However, in the case of EDXR, a single collection is usually sufficient to obtain a pattern containing the information required on the sample, and the problem of multiple acquisitions is overcome.

A last drawback usually attributed to the ED mode is the complication of experimental data processing.

The use of a white radiation, rather than a single energy beam, requires a normalization to the incident energy spectrum and a separate treatment of each energy component in the data processing. In the same way, the effect of all those unavoidable, energy-dependent phenomena that accompany elastic scattering (absorption, polarization, inelastic scattering) must be taken into proper account.

In particular, when the Parratt equation is applied to fit reflectivity data of stratified samples, attention must be paid

to the dependence on λ^2 of the real part δ of the refraction index, since the attribution of a constant value to it induces systematic errors. Indeed, the q dependence of an energy dispersive experiment is slightly different compared with that of an angular dispersive one (q^{-6} rather than q^{-4}), since such a λ^2 term corresponds to an extra factor proportional to q^{-2} ($q \propto 1/\lambda$ equation (3.1). Fortunately, such errors are usually very small, as demonstrated in [74], where the effect of a fixed value for δ was estimated in the energy range of interest 8.04–17.44 keV. Indeed, although δ actually varied by 4.37 times in such a range, the errors induced were negligible.

In conclusion, provided that the variable energy involves some complications in data processing, the situation is much more favourable for reflectometry than for diffractometry, since the effect of the absorption (due to the thinness of the sample) is usually small and often negligible, as is the polarization effect (see section 2). Moreover, as already discussed, the inelastic scattering is almost absent, being vanishingly small at low q values [67].

Conversely, the advantages of ED over the AD technique are of extreme importance, especially when real time studies are carried out.

The most important advantage consists of the fixed geometry setup. Owing to this, the footprint of the beam on the sample is constant and no data renormalization to the irradiated surface as a function of q is necessary. It must be noted that the longitudinal size of the footprint is $1/\sin\vartheta$. Therefore, in the AD mode, due to the grazing incidence, the part of the sample which is irradiated may vary remarkably and inhomogeneity and boundary effects may occur. Furthermore, if time-resolved measurements are carried out, the repeated mechanical movements necessary in AD may compromise the reliability of the experimental data. Indeed, in the critical conditions required for reflectivity, even minimal misplacements or misalignments may result in serious errors in measurement. As mentioned above, some AD reflectometers can be equipped with an array of counters (or with an image plate detector), sharing with ED the characteristic of having a static geometry. However, this possibility is not considered here because of the symmetrical setup required to guarantee that the reflection angle equals the incidence angle. Some attempts were made by using a divergent beam but the results were not particularly encourageing [75] (see below).

In XR measurements, the sample under study is often the component of a device (this is actually one of the most interesting future applications of EDXR, see section 5). The device may not have been conceived to allow x-ray measurements and, therefore, may be far from being an ideal sample container for reflectivity investigations. Fortunately, in ED it is sufficient to find two fixed paths across the device (one to irradiate the layer of interest by means of the primary beam and one to collect the reflected radiation) to perform the measurement. These two paths are much easier to find than two whole angular intervals, as required in AD.

Actually, the EDXR technique was not the first to be used in order to carry out *in situ*, fixed geometry x-ray reflection measurements. A first rough method consisted of selecting, in sequence, several fluorescence lines (in this case, by replacing the tube anode) and collecting the reflected intensity by a (non-dispersive) detector. In this way, the reflectivity pattern

can be sampled in correspondence with a discrete number of the momentum transfer values according to equation (3.1), providing some piece of information regarding the reflectivity characteristics of the sample.

Subsequently, a different approach was tried for the same purpose, namely the utilization of a monochromatic, but slightly divergent, x-ray beam to perform reflectivity investigations using a static setup.

The beam was sent to the sample and the reflected radiation was collected by an image plate detector. The divergence allows for the measurement of a section of the reflectivity pattern in the q-range, ($q_1 = aE\sin\vartheta_1, q_2 = aE\sin\vartheta_2$), where ϑ_1 and ϑ_2 are the minimum and maximum inclinations of the x-rays, respectively. Also in this case, no movement of the experimental apparatus is required during data collection [47]. Nevertheless, these techniques represented only interesting attempts, not being by far so flexible and reliable as EDXR.

Another merit of ED is a consequence of the multiplex data collection which it utilizes. In the AD method, the spectrum points are collected in sequence, with a scanning rate that is determined by the rotation speed of the x-ray machine arms. The ED method, instead, permits acquisition of the data points in parallel, i.e. simultaneously at each q value. Therefore, the reflection at any q value inside the accessible reciprocal-space window is visible in real time so that the acquisition can be stopped when sufficient statistics is reached in the regions of interest, for instance, when the signal-to-noise ratio for a given peak exceeds a certain threshold [9].

In static investigations, the two alternatives (sequential versus parallel collections) are equivalent but, if the sample is undergoing a transformation, the ED can be more reliable. In ED, the time resolution is given by the collection time of the reflection patterns and the morphology depicted by a single pattern corresponds to the average state assumed by the sample in the acquisition time interval of that pattern. On the other hand, if the sample changes its morphology during AD acquisition, the low q-values will be relative to the morphology assumed in an evolutionary stage preceding that described by the high q tail, inducing systematic errors in the fit.

A final quality of ED should be mentioned. It is connected to the continuous spectrum used in ED as a primary beam in comparison with the fluorescence line used as primary beam in AD. In typical working conditions, the ratio between the integrated intensity of the continuous spectrum and the intensity concentrated in the fluorescence line spans from one to two orders of magnitude. Since the reflected intensity is proportional to the incident intensity, the saving of acquisition time (at a parity of statistical accuracy) is significant.

To conclude the discussion on the ED technique, an outline of ED x-ray machine components and the effects that must be taken into account for the data processing are described. If the reader requires, more details can be found in the references that are quoted [67].

3.2. The EDXR measurement: instrument and experimental technique

At a first glance, an ED reflectometer looks like a commercial AD reflectometer. It is composed of an x-ray tube, a
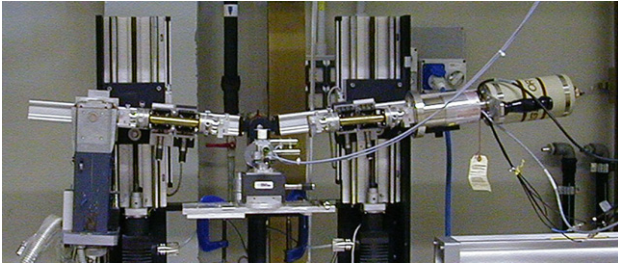
Figure 5. Sketch of the energy dispersive x-ray reflectometer. The fundamental components are as follows: (1) x-ray source (W anode tube), (2) collimation slits, (3) sample holder and (4) Ge single crystal energy-sensitive detector.

collimation system, motors to rotate its arms, a sampleholder to adjust both the position and the inclination of the sample and a detector, as visible in figure 5 [76].

However, there are a number of basic differences.

– The ED machine does not have a monochromator to select a single energetic component from the radiation emitted by the source. The un-monochromatized radiation is sent directly onto the sample through the upstream collimation slits, the fluorescence lines superimposed to Bremmsstrahlung not representing a problem. The reflected radiation is collimated again by the downstream slits that define the detector acceptance angle.

– The rotating system is not equipped with a high precision goniometer, since no continuous scan of the angles is necessary. To accomplish an EDXR measurement, it is sufficient to predetermine with accuracy the inclination of the arms corresponding to the angle (or to the set of angles, if several q-ranges are to be explored) at which each pattern collection has to be carried out. From this point of view, the motorization is just an optional function.

– The detector is the characteristic feature of an ED x-ray machine. It must be able to count the photons and to discriminate the energy of each of them. Solid state detectors whose sensitive component is a Si or Ge photodiode are generally utilized. The photodiode is inversely polarized at a high voltage in order to have a thick depletion zone. The electron–hole pairs produced in this zone, either thermally or by an external ionizing agent (charged particle, radiation, etc), are immediately separated by the strong electrostatic field present and move towards the opposite ohmic contacts. To decrease the thermal contribution to the electron–hole current reaching the contacts, the semiconductor crystal is cooled by a liquid nitrogen bath or by a cryostatic fluid.

When an x-ray photon is absorbed inside the active layer of the diode, many processes can be activated by the high amount of energy released to the crystal. However, the initial excitations tend to redistribute their energy in a great number of less energetic excitations. The redistribution ends when the lowest energy excitations, i.e. the creation of electron–hole pairs, are activated. The consequent migration of the electrons and holes to the ohmic contacts produces a current pulse, whose integrated intensity is proportional to the number of pairs and, therefore, to the energy of the absorbed photon. To calculate this energy, the pulse is sent to an integrating circuit

after being amplified and conveniently shaped. The subsequent stage of the electronic chain, an A/D converter, attributes a numerical value to the incoming charge and communicates this value to a multi-channel analyser (MCA). The MCA displays the information obtained from the detection system. Schematically, it plots a frequency histogram, the horizontal axis having a discrete index (channel) that identifies an energy interval and the vertical axis having the number of recorded events whose energy is contained in each interval.

Therefore, the detection mechanism can be summarized as follows. When a photon is captured in the active layer of the diode, the current pulse generated brings the information on the photon energy to the MCA. The latter increases by a unit the value relative to the channel corresponding to the photon energy.

Besides the electronic chain noise, the energy contribution to the uncertainty on q (see equation (3.2)) is due to the intrinsic fluctuation of the statistical detecting process. Indeed the number of pairs produced is a stochastic variable, whose average value is proportional to the photon energy. The absorption of a sequence of photons having the same energy corresponds to the sampling of the distribution function of such stochastic variable. For this reason, the measurement of a monochromatic radiation does not appear on the MCA as a Kronecker δ line but, rather, as a dumbbell distribution whose width increases with energy. Furthermore, this distribution is asymmetrical, the left front having a longer tail than the right, because some of the pairs created may recombine, thus subtracting a fraction of the charge to the current pulse.

The relation between the energy and the channel index is linear and, once the electronic system is set, its coefficients can be calculated by a convenient fit, for instance using a sequence of fluorescence lines (whose energy is known) as calibrants.

To perform a reliable EDXR measurement, a few precautions must be taken in the use of the detection system just described in order to prevent possible systematic errors. The precautions are connected to the non-ideal behaviour of the system. Indeed, some undesired effects occur during the detection process, which might modify the acquired patterns slightly. The impact of these effects is generally very low in a reflection measurement, being relevant only when intense signals are present in the spectra, which is rarely the case of reflection patterns (above critical point).

3.3. Escape effect

The main mechanism of photon capture in the active crystal of SSD is photoelectric absorption. In the subsequent disexcitation, the ionized atom may emit a fluorescence photon. Since the energy of the fluorescence photons of an element is a little lower than the ionization energy of that element, they have a rather long free path and, hence, an appreciable probability of escaping outside the crystal.

If we call E_0 and E_f the energies of the captured (primary) and emitted (secondary) photons, respectively, when the secondary photon succeeds in escaping, an energy $E_0 - E_f$ will be attributed to the primary photon instead of the correct energy E_0. The escape probability is a function of E_0, which can be calculated theoretically on the base of the crystal shape and the interaction cross sections of the element forming the

crystal (Si or Ge). However, from a practical point of view, it is easier to carry out a preliminary calibration of the detector, by measuring the ratio R between the intensity at E_0 and that at $E_0 - E_f$. In order to do this, the same sequence of fluorescence lines used for calibrating the MCA can be utilized or, alternatively, the Bragg peaks of a single crystal. Once a set of R-values is calculated in correspondence to several E_0, the whole $R(E_0)$ function can be obtained by a convenient fit.

3.4. Pile-up effect

The previous mechanism depends on the escape probability only and, therefore, on the total number of photons detected at a certain energy, while the pile-up effect is a function of the absorption rate of the photons. As discussed above, the capture of a single photon produces an electron–hole current pulse, whose integral over time allows the photon energy to be determined. However, if two photons having energies E_1 and E_2 are captured at a short time distance, the corresponding current pulses may be partially overlapped and the electronics may not be able to distinguish them. In this case, instead of two photons, the system interprets the overlapped pulses as a unique pulse to which the energy $E_1 + E_2$ is attributed.

These two effects act on the spectral profile in opposite ways: the escape effect induces an increase in the observed intensity at energies lower than the real one and the pile up at energies higher than it.

Another difference is that the escape contribution is fixed, depending on the geometry and on the material of the diode only, while the pile up depends on the radiation intensity at each energy.

Let us examine the relevance of the two effects on the reflection patterns.

A reflection pattern is characterized by the initial plateau of total reflection and, above the critical q value, drops down as q^{-4} or even more rapidly, depending on the roughness of the sample. Remarkable escape effects must therefore be expected below q_c, which is not usually a region of interest, or in correspondence with superlattice Bragg peaks, whose intensity may produce some satellite escape peaks. However, such Bragg peaks appear because of the semilog plot generally chosen for displaying the reflection patterns. When shifted to lower q by a quantity corresponding to E_f, these peaks would appear much lower due to the slope of the reflection pattern profile. This is even more true for their escape peaks, whose intensity is just a small fraction of that of the parent peaks. For this reason, only rough corrections are required, sophisticated methods not being necessary. If the system under study is not a superlattice, the correction can be omitted completely with no significant consequences.

The situation is a little different for the pile-up effect. This is because the spurious contributions are localized at energies higher than those of the photons producing them. Photons below q_c may therefore produce a fictitious increase in the region above q_c, with a consequent distortion of the pattern. To minimize this problem, x-ray filters can be used. Indeed, a metallic foil, whose optimal thickness must be determined as a function of the profile of the incident beam spectrum, of the reflection angle and of the critical parameter of the material, can be used to cut the low energy part of the beam spectrum,

thus preventing the total reflection intensity from getting too high. Another way to reduce the pile-up effects consists of decreasing the shaping time of the amplifier, so that a higher number of photons per unit time can be processed before the energy spectrum distortion becomes significant. This is particularly useful if an intense synchrotron radiation emitted by a bending magnet is utilized as a primary beam [73].

To conclude, two other spurious contributions, which are due to the sample rather than to the detection system, are worth mentioning.

3.5. Fluorescence lines and absorption edges

The sample or the substrate may absorb a part of the incident beam. The subsequent corresponding edges and fluorescence emission will be detected as extra features superimposed on the reflectivity spectrum. However (unlike diffraction, where the fluorescence lines can be confused with Bragg peaks), they are much sharper than any superlattice peak and can be easily cut without further cautions. On the contrary, the presence of an absorption edge may be critical, since it may cause a distortion of the reflection profile. Difficulties may arise when the studied samples are characterized by layers of different densities (see, for example, section 6.2 on organic solar cells). Nevertheless, also in this case, the problem is not serious, because the distortion is localized in a narrow energy interval. Since the fit is extended to the whole reflection curve, a local distortion does not induce big errors. Furthermore, if a very accurate determination of the fit parameters is required, a way to overcome the problem consists of collecting two reflection spectra at two different angles. Indeed, if the choice of the angles is appropriate, after the conversion of the energy into the scattering parameter (according to equation (3.1)), the two spectra can be linked up forming a unique pattern in which the zone where the distortion occurs has been excluded.

3.6. Small angle scattering contribution

The reflectivity measurements are accomplished in experimental conditions analogous to those of small angle x-ray scattering. Broad SAXS peaks may, in fact, fall in the same q-range, producing a strong distortion of the reflection pattern. If the thicknesses of the layers constituting the sample are not known, it is possible to interpret the broad peak observed as the Kiessig fringe of one of the layers (a very thin one). Since the SAXS cross section is very small, the peak can only be produced by the substrate. Hence, a measurement carried out on the naked substrate in the same conditions will provide the necessary correction.

3.7. Sample alignment

To align the sample for a reflectivity measurement, a simple protocol has to be followed. Indeed, placing the sample in the centre of the reflectometer by hand does not guarantee that it is at the right height and with the right inclination. The correct position can be found by a three-step procedure:

(1) The arms are placed horizontally, (direct transmission, $\vartheta_1 = \vartheta_2 = 0$, figure 6(a)), and the film is raised vertically until the primary beam is intercepted by the sample, so
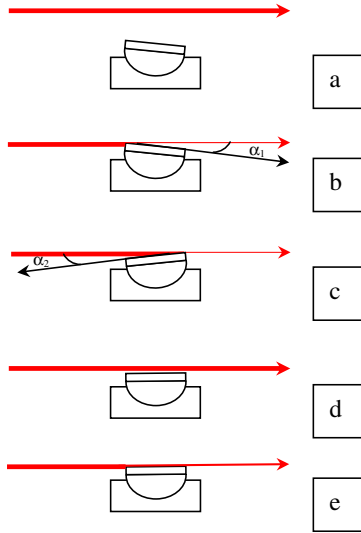
**Figure 6.** Schematic drawing of the alignment procedure.

that just a very small intensity is visible at the detector (figure 6(b)).

(2) Starting from this initial angular position α_1, the sample holder's cradle is tilted in the direction corresponding to an increase in the intensity observed at the detector. The intensity will reach a (maximum) stationary value inside a certain α-interval and will then decrease again. The tilt can be stopped when the observed intensity equals the initial intensity. Calling this extreme position α_2 (figure 6(c)), the average angular value between α_1 and α_2 corresponds to the condition of parallelism between the primary beam and the sample surface (figure 6(d)).

(3) The sample is raised again until a small fraction of the beam is intercepted, so that the rest laps the surface. At this point the reflectometer arms can be inclined symmetrically at the working reflection angle and the measurement can start.

A last remark is opportune on this subject. The above procedure can be affected by small systematic errors. If the sample is not in the centre of the machine, a symmetric rotation of the arms does not correspond to a perfectly specular geometry. Therefore, after the arms are inclined, a further small adjustment of the sample inclination, consisting of maximizing the reflected intensity, is recommended. However, it is worth stressing that, in ED, only a single reflection condition is required. Therefore, once a suitable reflection condition is found, the measurement can be carried out even if the sample is not placed in the ideal position. Instead, in AD, the variable geometry requires that the sample is accurately centred and aligned, otherwise the specularity is lost along the angular scan.

3.8. Calculation of the sample density

Despite the former procedure, minimal residual deviations from the ideal specular condition may occur. If x-ray reflectivity is used to performed density measurements, these deviations may result in relevant errors on the density value and a further calibration is recommendable.
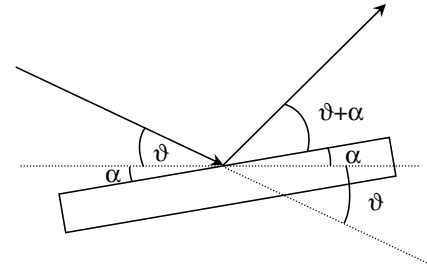
Figure 7. Schematic drawing representing the experimental conditions of an x-ray beam reflected by a non horizontal surface. The misalignment induces an error on the measured electron density.

The error on the density can be calculated following the method proposed by Windover *et al* [77, 78] and based on a multi-wavelength approach to x-ray reflectometry.

Let us suppose that the primary beam direction forms an angle $\vartheta + \alpha$ with the sample surface (figure 7) instead of the nominal angle ϑ and that, nevertheless, the acceptance angle of the detector is wide enough to allow the collection of the beam reflected at $2(\vartheta + \alpha)$. In this case, the (true) momentum transfer q_t equals $[aE \sin(\vartheta + \alpha)]$, rather than $[aE \sin \vartheta]$, which is the supposed value (q_s) calculated on the base of the nominal setup parameters. In particular, this applies to the critical value q_c.

Since α is small in comparison with ϑ, q_t can be approximated with its expansion at the first order in α: $q_t \cong aE(\sin \vartheta + (\mathrm{d}\sin \vartheta / \mathrm{d}\vartheta)\alpha)$. From (2.4), the electronic density is proportional to q_c ($N = (q_c^2/16\pi r_0)$), so that the relative error on the density induced by the error on the angle is

$$\frac{N_t - N_s}{N_t} = \frac{q_{c,t}^2 - q_{c,s}^2}{q_{c,t}^2},$$

where the suffixes 't' and 's' stand, again, for 'true' and 'supposed'.

Substituting the expressions for $q_{c,t}$ and $q_{c,s}$,

$$\frac{N_t - N_s}{N_t} \cong \frac{[aE_c(\sin \vartheta + \alpha \cos \vartheta)]^2 - (aE_c \sin \vartheta)^2}{[aE_c(\sin \vartheta + \alpha \cos \vartheta)]^2}$$

$$\cong \frac{2\alpha(aE_c)^2 \sin \vartheta \cos \vartheta + o(\alpha^2)}{(aE_c)^2 \sin^2 \vartheta + o(\alpha)} = \frac{2\alpha}{tg\,\vartheta} + o(\alpha^2),$$

where $o(\alpha)$ and $o(\alpha^2)$ are terms of the first and second order in α and can be neglected.

In conclusion, the relative error on the density is about $2\alpha/\vartheta$ (with α positive or negative). In practical cases, α can likely be a few per cent of the reflection angle and the error on density twice as much. When accurate determinations are required, for instance if components of electronic devices are to be investigated, such an error may not be acceptable and a further calibration is necessary to reduce the asymmetry.

In order to do this, the equivalent of a diffraction rocking curve has to be carried out, i.e. a scan of the in-plane component q_x of the total exchanged momentum $\boldsymbol{q}$. Experimentally it consists of acquiring the reflected intensity as a function of the asymmetry angle α ($q_x = aE \sin \alpha$).

As an example, the reflection rocking curve of a film is shown in figure 8.

It can be noted that the patterns show an almost symmetric behaviour with respect to the central one, which individuates the specular condition. In order to show the effect of an
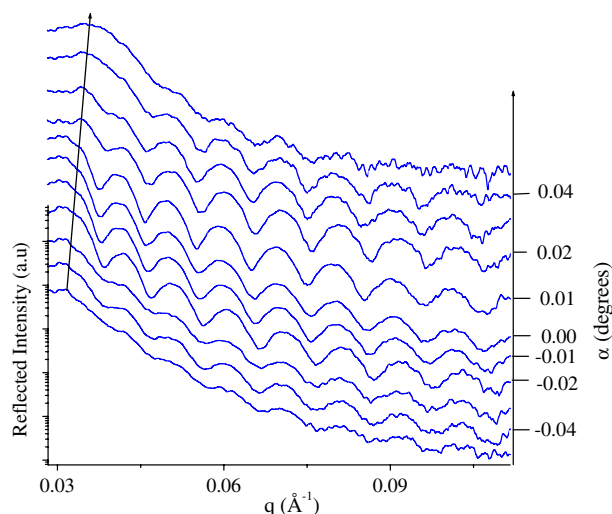
Figure 8. Sequence of EDXR patterns collected as a function of the scattering parameters and of the asymmetry angle α. The arrow evidences the shift of the critical reflection edge towards higher q values.

incorrect positioning of the sample, the momentum transfer was calculated neglecting the extra term $[(aE\cos\vartheta)\alpha]$. As a consequence, the critical edge seems to shift. From figure 8, it appears that the reference value ($\alpha = 0$) does not correspond to the central pattern, which is located, instead, at about $\alpha = 0.01$. Therefore, the latter value must be assumed to correspond to the real specular conditions and the offset considered in the calculation of q. However, this effect can be revealed owing to the comparison of the patterns collected at various α. If only a single pattern was measured, the above extra term could not be identified and the systematic error could not be corrected.

3.9. Data processing

While the discussion on data correction and processing occupies much space in EDXD papers, owing to the simplifications allowed by EDXR, just a few operations are required and the following short description is sufficient.

The raw reflection spectra collected (besides being corrected for the undesired effects concomitant to reflection) must be normalized to the incident radiation spectrum. The latter should be collected in conditions similar to those in which the reflection measurement is carried out, otherwise distortions are likely to occur. The methods adopted to measure the white beam spectrum [67] both direct (extreme collimation, reduction of the power supply current to μA) and indirect (by means of filtering, scattering from a noble gas, total inelastic scattering, etc) are all unsuitable to some extent. Each of them provides a white beam spectral profile with slightly different characteristics, and the relative normalization procedure is not able to reproduce a perfect plateau in the reflection pattern below q_c. It was found that a method that guarantees the perfect flatness of the plateau region and no distortion (also in the rest of the reflectivity profile) is the simplest one. It consists of normalizing the pattern by a second reflection pattern collected at a lower angle, so that q_c is sent out of the right-hand side of the selected q-space window, that is to say, the maximum q-value observable at that angle is below q_c. In the latter case, the reflectivity equals unit at any q value and, hence, the second

pattern reproduces the incident beam profile exactly. In such a case, the working setup is almost the same in the first and second reflection measurements. Indeed,

- just a small decrease in the reflection angle is usually sufficient to meet the total reflection conditions for the collection of the second pattern, so that the setup geometry is almost unchanged;
- the arrangement of slits is unchanged;
- even minimal systematic errors induced by an imperfect instrumental geometry will be reproduced in the second pattern and compensated by the subsequent normalization.

Of course, the white beam measurement carried out as discussed above must be carefully performed, because, at such very low angles, problems analogous to the ones occurring with SAXS may arise (namely, the collection of a part of the incident beam that falls inside the acceptance angle of the detector).

Finally it must be stressed that, due to the fact that the reflection patterns are normalized to the primary beam spectrum, the energy response function of the detector drops out of the reflectivity calculation.

3.10. Subtraction of the diffuse scattering

Although in specular conditions the contribution of reflectivity to the detected signal is dominant, diffuse scattering also has its maximum value there. To isolate the reflectivity profile, the diffuse scattering contribution must be evaluated and subtracted. The rocking curve measurement described above for density determinations can be also used for this purpose. The off specular diffuse intensity is collected during an α scan (excluding $\alpha = 0$ where the diffuse signal is superimposed to the specular reflectivity one) and can be calculated by a fit of the data collected at $\alpha \neq 0$.

In ADXR, this method would imply a very long procedure, since a complete α-scan (q_x-scan) should be accomplished in correspondence with each ϑ (i.e. each q_z), exactly as is done in diffraction, to plot the rocking curve of a Bragg peak of a crystal. However, while the diffraction patterns are characterized by a discrete number of Bragg peaks (i.e. a discrete number of ϑ_i), separated by 'zero intensity' zones, the reflectivity patterns are continuous. Fortunately, in EDXR, instead, for each α-value the whole reflection pattern is collected in a single measurement; namely, the rocking curve is measured in parallel for all the q_z-values. This characteristic makes the reflection 'rocking curve' practically possible and enables the reflectivity profiles to be calculated precisely, free from diffuse scattering contributions.

However, the diffuse resonant x-ray scattering can also be used as a tool to detect interface roughness and the lateral dimension of the scattering domains. In [79], the authors accomplish EDXR measurements to gain information on the thickness of Langmuir–Blodgett multilayers of lead stearate, but they deepen their investigation slightly changing the 1 : 1 ratio of the incident and reflected angle to measure the diffuse part of x-ray scattering. Owing to the energy dispersive arrangement (Mo x-ray Tube, Si(Li) detector, 3 KeV $< E <$ 40 KeV), the measurement was easily performed at three different values of the incidence angle, keeping the angle between detector and primary beam unchanged. Due to the in-plane roughness

correlations of the interfaces, the diffused scattering is modulated (as in the specular measurement) and exhibits peaks. The slope of the peaks intensities as a function of the asymmetry parameter provides the lateral correlation length.

3.11. Further uses of an appropriate angular setup

The quality of EDXR of having an extra degree of freedom represented by the variable energy of the photons can be used, as discussed above, to solve problems arising from samples absorption edge and fluorescence emissions. However, it can be applied, as well, each time that is necessary to shift the reflection pattern along the multichannel, namely along the energy scale. Indeed, each point of the pattern corresponds to a certain q-value, which is proportional to the product $E \sin \vartheta$. Therefore, a change in the reflection angle will be counterbalanced by an opposite change in the energy at which that point appears. This possibility can be used, for instance, to observe the anomalous Bragg reflections in the neighbourhood of an absorption edge. By decreasing the reflection angle, it is possible to move the Bragg peak under investigation from below to above the edge. After normalizing to the incident white spectrum, the difference between the obtained reflection patterns will provide the contribution due to anomalous components of the scattering amplitude $\Delta f'$ and $\Delta f''$. Indeed, while other peaks appearing far from the edge are unaffected by the slight angular change, the one passing through the edge suffers a relatively large modification of the energy-dependent $\Delta f'$ and $\Delta f''$. In this way, the tools for anomalous x-ray diffraction can be applied and specific information on the element can be gained.

With reference to what has been discussed so far, when a comparison between the ED and the AD techniques is made, it appears that the drawbacks of the former are of minor importance, while the advantages can be fundamental for simplifying (or even to allow) several of the most useful kinds of investigations possible by laboratory x-ray reflectometry.

In the following section, a review of the papers published relating to this subject, which focus on the most interesting and peculiar aspects of each of the reported studies, is made.

4. EDXR for chemical investigations: electron density determination

The EDXR technique, as discussed, may be useful in the determination of films densities. As an example, in [32] this method is used to evaluate the percentage of CH_4 molecules on functionalized Si. In this case, the determination is based on the relative variation of the Si reflection edge, assumed as an internal standard. The measurements were performed using the white beam produced by an W anode x-ray tube (55 kV–25 mA) and a high purity Ge single crystal solid state detector accomplished the acquisition. The experimental geometry was kept unchanged (collimation slits, scattering angle, beam divergence and dimension) during the collection of the reflectivity patterns on the differently coated films. The repositioning of the samples, after each acquisition, was accurately reproduced in order to minimize misalignment errors and to allow maximum reproducibility.
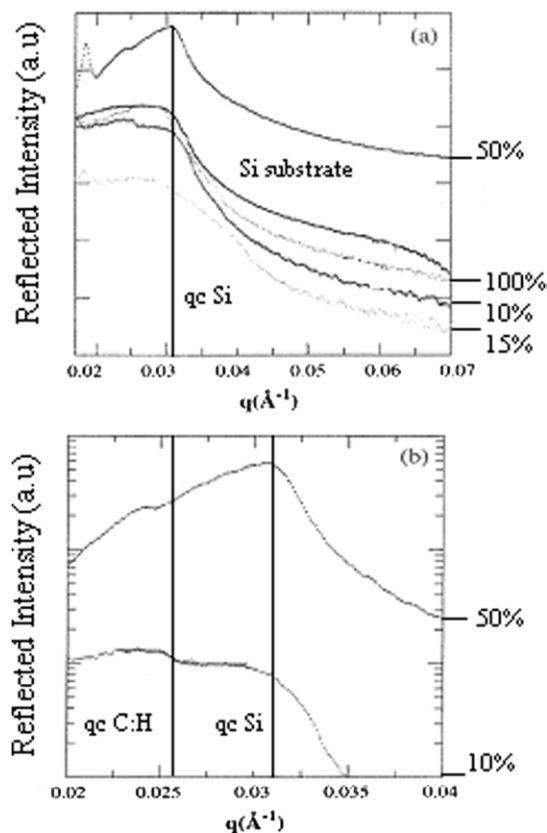
Figure 9. (a) Si Reflectivity patterns were collected to detect the critical edge and are shown as a function of the scattering parameter. The percentage of surface –C : H coverage is reported for each spectrum. (b) The reflectivity plateau is highlighted in the case of the 10% covered sample and the 50% covered sample. In both cases, a novel edge is visible and can be attributed to the –C : H.

The critical scattering parameter of the Si wafer was calculated by fitting the EDXR patterns, to test the accuracy of the measurements compared with values reported in the literature, and good agreement was found (figure 9(a)). The second step consisted of the measurement of differently coated a-C : H Si substrates. At a low coating percentage, the presence of CH_4 molecules induces a modification of the characteristic Si edge shape (figure 9(a)), but as soon as films are obtained with a CH_4 concentration of 10% (or higher), a second reflection edge, which can be attributed to the CH_4 molecules, appears.

In figure 9(b), the reflectivity profiles of two films with 10% and 50% of CH_4 molecules content are shown, respectively. In these cases not only the Si reflection edge can be fitted but the critical scattering parameter related to CH_4 can also be deduced. Comparing the critical parameters related to CH_4 in those two films, $q_{c10\%} = 0.0256\,\text{Å}^{-1}$ and $q_{c50\%} = 0.0242\,\text{Å}^{-1}$, respectively, the authors assume the latter film to be less dense. Indeed, with a good approximation, the critical scattering parameter is directly proportional (considering the scattering volume to be constant) to the electron density square root and thus to the material density. This information, deduced by EDXR density determination, was confirmed further by the authors using other techniques (SAXS, ellipsometry and FTIR).

5. Investigation of the morphological properties of layered systems and devices

5.1. x-ray mirror surface morphology investigation

5.1.1. Part one. In 1982, the first energy dispersive x-ray reflectivity experiment reported in literature was performed by Bilderback and Hubbard [33]. The purpose of their study was to measure the reflectivity of x-ray mirrors over a wide range of energies and many orders of magnitude. Indeed, according to what has been discussed, a mirror at a fixed angle reflects, with high efficiency, wavelengths that are longer than the critical one and rejects (transmits) the x-rays having wavelength shorter than the critical one. This kind of mirror is often used as a focusing device and has traditionally been studied from the very soft end of the x-ray spectrum, up to about 10 keV. The authors have extended the experimental measurements to the 50 keV region. The ED x-ray reflectivity is particularly useful in this case, since it allows one to directly observe the rejection efficiency of the higher order harmonics of a given fundamental frequency.

To perform the x-ray total reflection measurements, two x-ray sources were used: a silver anode tube operating below 20 keV and a tungsten anode x-ray tube operating up to 50 keV.

Float glass mirrors of two different thicknesses (0.23 and 0.18 nm) were studied to observe the effect of the surface roughness (induced by a HF etching) on the x-ray reflectivity.

At first a series of measurements were performed on the 0.23 cm thick mirror at various angles (0.7, 1.2, 3.5 and 5.6 mrad). As expected, despite the different geometrical configuration, the morphological response of the mirror was the same. It consisted of a reflectivity plateau up to the critical energy, followed by a sharp fall in the reflectivity profile. This property allows the use of a sheet of flat glass as a low pass filter, the reflectivity critical edge corresponding to the cut-off value. The authors investigated whether the shape of the reflection curves could be affected by changing the surface smoothness of the mirror or not. For this reason, the same mirror (0.23 cm thick) was etched for 2 min in 9 parts H_2O and 1 part HF acid by volume, and then, after the reflectivity measurement was performed, it was heavily etched, for 1 min in concentrated HF.

After the first light etch, the reflectivity profile was clearly modified, the spectra dropping much faster than the unetched mirror, indicating a significant increase in the surface roughness. This increased slope enhanced the harmonic rejection capability of the mirror by a factor of about 2.5.

Finally, after the heavy etch, the glass sheet was deteriorated, and the reflectivity was now diffused over a wide angular range (ca 5 mrad), i.e. the mirror lost its properties as filter.

These experiments were reproduced on a 0.18 cm thick float glass sheet, and the results were significantly different. In this case the mirror initial roughness was significantly higher and the light etching induced on the surface of this thinner sample a smoothing effect. Therefore, the slope of the reflectivity profile after the critical edge decreased, and consequently the mirror's harmonic rejection capability decreased too.

In conclusion, the authors showed that etching can either enhance or reduce the roughness of a mirror, depending on the original roughness, strongly influencing the harmonic rejection ability of the mirrors.

5.1.2. Part two. The experimental method described above was extended [34] to the study of other materials as a platinum coated mirror and a commercial silicon wafer. The first mirror was made by evaporating a 500 Å thick platinum coating over a fused silica polished flat glass. The EDXR patterns, measured over four orders of magnitude in intensity and up to 50 keV in energy, are qualitatively different from the ones of part I for their intensity is lower, at a parity of energy cut off. This is due to the stronger absorption effect of the Pt particularly in the vicinity of the Pt absorption edge. Moreover, in this case the sample under study is layered and the patterns are characterized by the presence of Kiessig interference fringes. The authors interpreted the data according to the Parratt model. Assuming the bulk density of platinum as a fixed parameter in the simulation, evident discrepancies with the data were observed, suggesting that the Pt layer density is 70–90% lower than the bulk one. The effect of the surface micro roughness is to produce a steeper decrease in the EDXR curve, with respect to the simulation relative to a smooth surface, resulting in a major harmonic rejection ability.

The possible use of a Si wafer as a single crystal synchrotron radiation x-ray mirror was also tested, in the same way.

In conclusion, the data obtained were in qualitative agreement with the theory and allowed the retrieval of information on the capability of platinum coated mirrors, commercial silicon wafers, rough surface aluminium, and copper and stainless steel of reflecting x-rays at small angles of incidence.

5.2. Determination of the thickness of thin films. Comparison with the AD technique

The measurement of the thickness of ultra-thin metal films represents an interesting challenge, being extremely useful in the development of future high performance devices (integrated circuits, low dielectric constant materials, diffusion barriers, etc).

In [35] an experimental comparison between EDXR and ADXR was carried out in the case of ultra-thin tantalum films. Various tantalum samples, deposited by sputtering on Si substrates, in a commercial sputter chamber, were studied. Extremely short deposition rates were needed to obtain very thin films, whose thickness was from 200 to less than 10 nm.

The three thinnest samples (8.8 nm, 13.4 nm and 23.8 nm, respectively) were measured both in the angular and in the energy dispersive mode, and in the latter case, the errors concerning the determination of the thicknesses were estimated.

For ADXR measurements, a single channel analyzer with a 300 eV collection window was used to measure the reflection patterns produced by a Cu k_α fluorescence radiation primary beam. The Cu anode tube was used in two different modes, at 10 kV, 10 mA as a low-intensity source and at 20 kV, 20 mA as a high-intensity source, respectively. The data collection was obtained performing $0.005°$ $\Delta 2\theta$ steps from $0.1°$ to $2°$ in 2θ.

In the case of the ED measurements, the Cu anode tube was set at 20 kV, 20 mA working conditions. The geometry of a commercial diffractometer was modified in order to obtain a maximum beam divergence of 0.043° in the reflection plane. The detector used was a Si-Type-Peltier-cooled Kevex detector connected to a Nucleus PCA II multichannel analyzer.

The reflectivity patterns of the thinnest film were collected both in angular and energy dispersive modes and the Parratt model was first applied to the AD spectra to obtain the most accurate information regarding film thickness, roughness and density. Starting from values obtained in this way, various fitting procedures were tested on the ED reflectivity patterns.

At first, the Parratt model was used keeping the density fixed on the 'true' value obtained by the AD measurement. The film's density was then varied and converged to a value which was quite different from the true one(16.6 g cm^{-3} and 8.3 g cm^{-3}, respectively), the discrepancy being attributed by the authors to energy dependent systematic errors. In this case, despite the significant difference of density, the thickness values could be estimated.

The results on several Ta films are reported in [35], showing that the error in the estimation of the film thickness due the incorrect determination of the density is always negligible (max. 3% when very thin films are concerned). This validates the use of Parratt simulations to perform the fitting of energy dispersive data for thickness and roughness determination.

Moreover, the use of the Parratt method may be time-consuming in some cases, since many parameters must be controlled in data analysis, and the estimation of the errors is not always easy. The authors propose a simplified model that can be applied when the film thickness is the only parameter to be deduced and a single layer with fixed uniform density is taken into account. This method is a development of the fast Fourier transform analysis for fixed angle data and the results obtained were roughly comparable to those calculated by the Parratt formalism, estimating an error which was double the real one (7% instead of 3% max.).

In another work [36] the results obtained both in laboratory and at the BESSY synchrotron radiation facility (the latter is not reported here, since we limited the review to laboratory sources) are presented to validate the use of such a technique in the study of phase transitions in thin films. In particular, a laboratory setup using a 18 kW rotating Cu anode generator was used to perform both ED and AD measurements on polymer and Langmuir–Blodgett thin films. Such results, shown in figure 10, demonstrate that the ED and AD reflection profiles are in agreement in the q range explored.

5.3. Gas sensor films

Organo-metallic thin films are widely investigated in view of their application as gas-sensing devices [80]. Indeed, their electrical properties change when the materials are exposed to particular pollutant gases (NO_2, CO_2, NH_3, etc). However it has been demonstrated that the morphological characteristics of these films (thickness and roughness) strongly affect the device's response and, therefore, may be determining factors to gain information on the gas–film interaction mechanism.

In [37], a first set of reflectivity measurements was performed on $(RuPc)_2$ thin films. In figure 11, the reflectivity
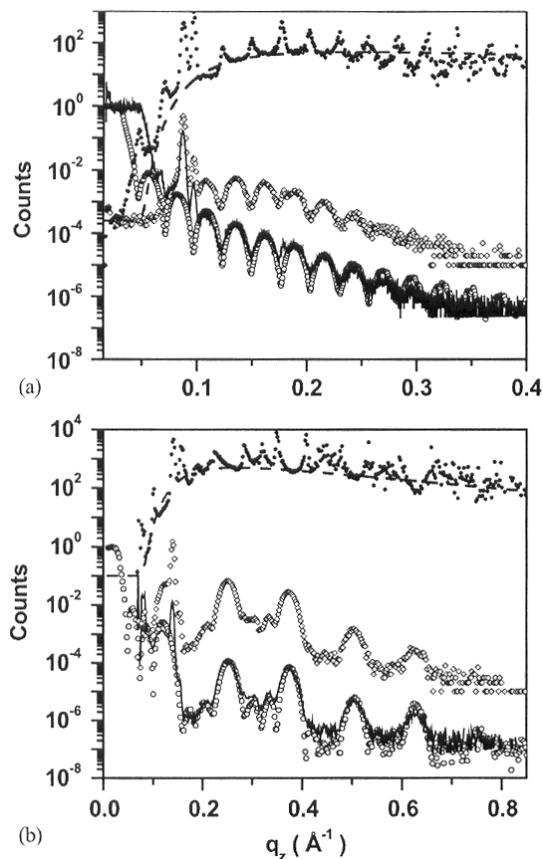
**Figure 10.** Reflectivity profiles collected upon a polymer (*a*) and a LB film (*b*) are plotted as a function of the scattering parameter together with the row energy dispersive data (open diamond). The upper curves in both (*a*) and (*b*) represent the $I_0(E)$ profile together with its fit (dashed line). Reprinted from [36]. Copyright (2004), with permission from Elsevier.

profiles (dots) of five samples (chosen as an example) are shown in semilog graphs, together with their Parratt fits (line). The white beam produced by a W-anode x-ray tube was used and the detection was accomplished by a high purity Ge single crystal solid state detector. As can be seen in figure 11, to carry out accurate data analysis, a wide q range was explored, performing more than one fixed angle ED measurement and then reconstructing the whole pattern by overlapping the spectra obtained at various angles.

Thickness and surface roughness were obtained fitting (straight lines figure 11) the reflectivity curves by the Parratt model, and a first observation was that the measured surface roughness statistically increased with the increase of the film thickness.

As a second experimental step, the authors exposed samples 2 and 4 (400 Å and 1000 Å nominally thick, respectively) to a NO_2 500 sccm gas flow (NO_2 100 ppm in air) for a couple of hours. The samples were then repositioned and re-measured to evaluate if their morphology showed any change due to the film interaction with the gas molecules.

The comparisons between the reflectivity spectra before and after the gas treatment were carried out normalizing the reflected intensity (above the q_c) to the Fresnel reflectivity of the Si substrate, in order to isolate the oscillating signal coming from the thin film only. Analysis of the data revealed that the
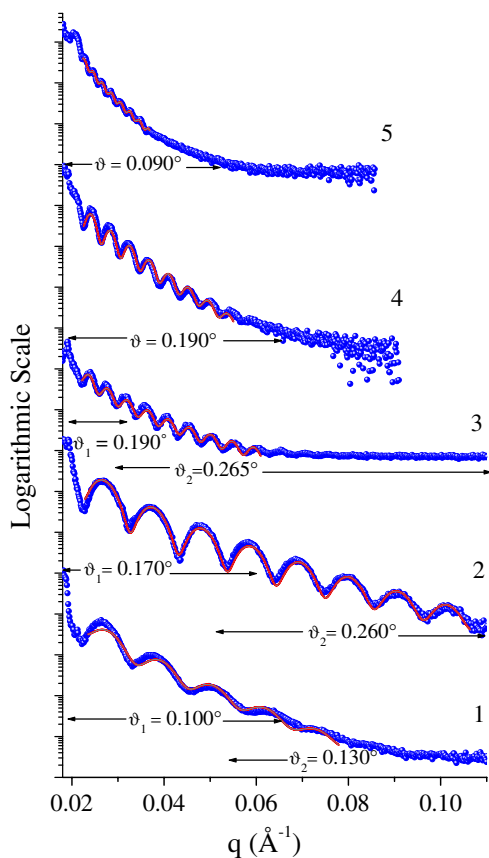
Figure 11. Total reflection measurements of ruthenium phthalocyanine thin films (dots) and calculated data (lines) as a function of the scattering parameter. The reflection angles chosen to perform the measurements are reported. Reprinted with permission from [37]. Copyright (2003) American Chemical Society.

Figure 12. The reflectivity pattern of the cyclohexane/water–CaCl$_2$ interface and model fit. Reprinted with permission from [38]. Copyright (1994) American Chemical Society.

film did undergo a change in thickness and roughness as a consequence of exposure to NO$_2$ gas.

The authors observed that an interaction, not restricted to the surface of the film only, had taken place. Indeed such an interaction cannot be described as an absorption or a chemisorption of a gas molecules layer confined on the film surface only, but it involves the film bulk as well.

Although the *ex situ* procedure, which consists of comparing the spectra before and after the exposure to the gas, can only give some clues regarding the mechanism of the process, in this preliminary analysis it was quite conclusive.

In particular the technique demonstrated that (RuPc)$_2$ films are sensitive to the NO$_2$ pollutant gas deserving more in-depth investigations (see section 6.1).

5.4. Tensioactives and surfactants on water

In 1994, Roser *et al* [38] presented the first EDXR measurements of an x-ray reflection profile from a liquid–liquid interface and, furthermore, demonstrated that the technique has the sensitivity and penetrating power required for buried interfaces measurements, usually performed at synchrotron beamlines. These measurements were performed using a W anode x-ray source and a germanium solid-state energy dispersive detector.

Two samples were chosen to demonstrate the feasibility of such energy dispersive experiments, both based on insoluble water/cyclohexane systems. Since the scattering length densities of the two components are rather close (0.940E−5 and 0.757E−5 Å^{-2}), a first experiment was performed adding a surfactant, namely calcium chloride hexahydrates (CaCl$_2$), to the aqueous phase. Subsequently, in a new experiment, a modified polyester surfactant, consisting of PEG 800 hydrophiles with fatty acid residues, was used. In this way, the difference in the scattering length densities was increased, thus enhancing the reflected intensity at higher angles.

The data were collected at four different angles in the case of the cyclohexane/water (CaCl$_2$) system. Once corrected for experimental factors, the spectra were rescaled and overlapped to obtain a single reflectivity pattern which spans over a wider q-range, as shown in figure 12.

In figure 13 the reflectivity profiles of the liquid interface are shown in the case of water–cyclohexane solution with the PEG surfactant: these data allowed the sensitivity of the technique to changes at the interface between two liquid components to be tested. As can be seen by the naked eye, in the present case the reflectivity profile decreases with q significantly faster with respect to the interface shown in figure 12.

The reflectivity profiles were fitted using the suite of FITLAY fitting programs [81] (figures 12 and 13, straight line). In the case of cyclohexane/water–CaCl$_2$, the scattering length densities of the aqueous and cyclohexane layers were kept fixed, while the interfacial roughness and the scattering background were used as free parameters. The interfacial roughness indicated by the data is virtually zero, i.e. less than 1 Å.
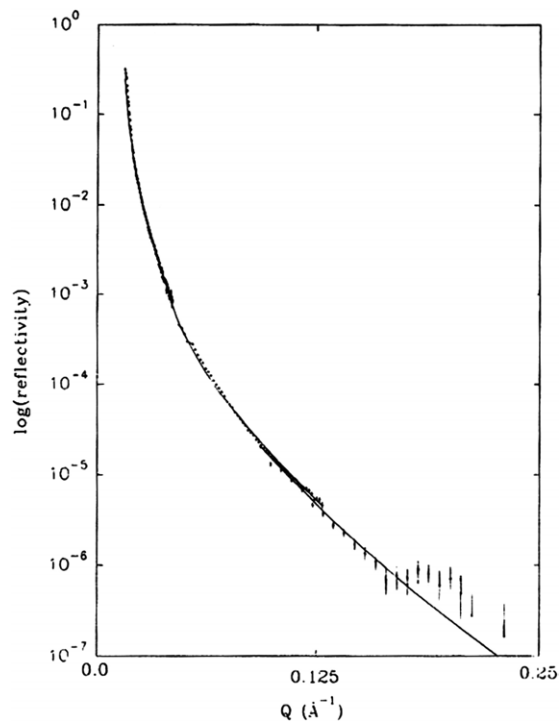
Figure 13. Reflectivity profile of the cyclohexane/water–PEG interface, and single layer model fit. Reprinted with permission from [38]. Copyright (1994) American Chemical Society.

In the second experiment, the thickness of the surfactant layer and the roughness of the hexane/surfactant and the surfactant/water were obtained. The data showed that there is clearly an excess of electron density associated with the surfactant at the interface. In general, the PEG chains are expected to extend into the aqueous phase and the aliphatic chains into the cyclohexane. This hypothesis was found to be consistent with the data on the aqueous side of the interface. Although a precise structure was not assigned to the adsorbed surfactant, these experiments clearly demonstrated the potentialities of the technique when liquid surfaces and interfaces are concerned, allowing the structural details of liquid–liquid interfaces to be investigated by an in-house setup.

5.5. Mesoporous materials

Mesostructured materials have potential applications for sensing, electrochemical and optical devices. Resistive sensor devices based on mesoporous silica thin film as a sensing membrane have been developed to detect both humidity and alcohol vapours in the environment [82].

In [39], the authors found a correlation between the deposition conditions and the response towards different relative humidity percentages. This correlation is due to structural/morphological changes occurring as a consequence of different growing conditions. Since these materials are mesoporous, they can be obtained by template and the templating surfactant is commonly eliminated by calcination of the films at different temperatures. Energy dispersive x-ray reflectometry was used to evaluate the variations in the dimensions of the pores in samples grown in different conditions (different calcination temperatures). In the case
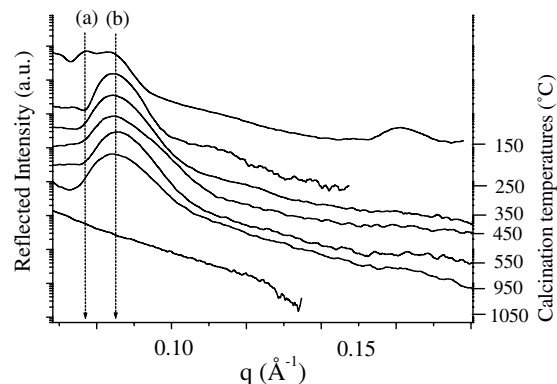
Figure 14. Reflectivity profiles of mesoporous silica thin films calcinated at different temperatures. (*a*) The position of this Bragg peak is related to the dimensions of the pores. (*b*) This Bragg peak corresponds to the surfactant agent still present at 150 °C in the film matrix.

of such materials, the reflectivity profiles are produced by the interference of the reflected beams due to the semi-infinite repetition of the same structure inside the film. In this case, the optical contrast can be attributed to the difference in the electronic densities produced by the alternation of the Si matrix and the empty pores. This repetition gives rise to the presence of broad Bragg peaks on the Fresnel reflectivity profile, and the dimensions of the pores can also be deduced, by evaluating the position of the peaks.

A systematic reflectivity analysis was performed in order to achieve morphological and long range structural information on samples of these materials, calcinated at various temperatures in the range 150–1050 °C. All reflectivity patterns were collected in the same conditions, at grazing incidence (teta = 0.125°) and in a controlled atmosphere (N_2 flux, 180 nmol s^{-1}). In figure 14, the reflectivity spectra are shown as a function of the scattering parameter and the intensities are rescaled to enhance the dependence on the calcination temperature.

It should be noted that the pattern of the sample calcinated at 150 °C differs from the others, since it exhibits an anomalous (convolved) double peak. Such a behaviour is related to the presence of two different ordered bulk systems having different scattering length densities. This gives rise to two signals: one related to the pores and the second to the surfactant that is still present at this low calcination temperature. As the temperature increases, only the signal coming from the mesoporous structure remains and the Bragg peaks become even broader, indicating that the internal order is decreasing due to the thermal treatment. Finally, at 1050 °C, no reflections are visible any longer, indicating the lack of a mesoporous structural order.

The surface roughness was calculated by the Parratt model for each reflectivity profile. All films exhibit a roughness value in the range 6–8 Å, except for the one calcinated at 1050 °C, whose value is as high as 13 (2) Å. This is further evidence confirming the disorder characterizing samples submitted to high calcination temperatures, not only in the bulk and also on the surface.

This work is an example of the use of EDXR to characterize both the morphology of thin films and also the internal structure of ordered materials.
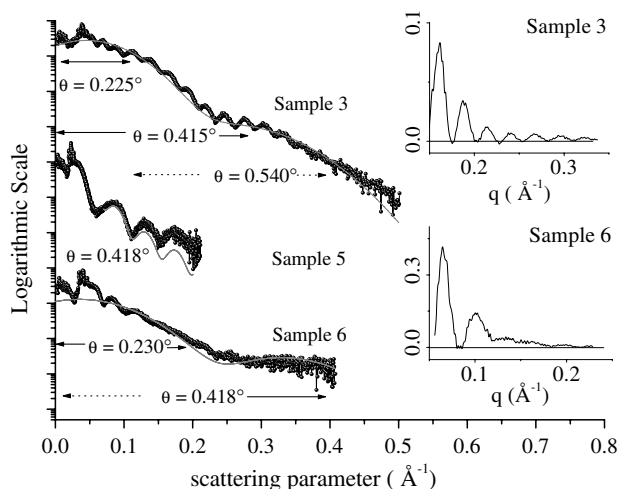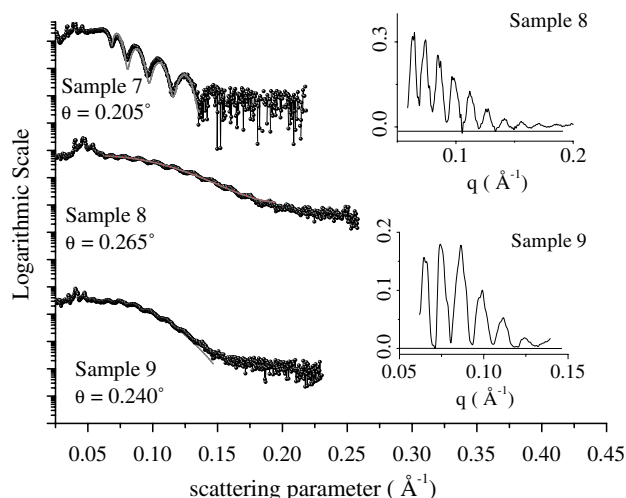
Figure 15. EDXR patterns of Cr/Pt films deposited on Si. In the insets, the contribution of the Cr film only is shown after the subtraction of the Pt cap layer signal. Reprinted with permission from [40]. Copyright (2004) American Chemical Society.


Figure 16. EDXR patterns of Cr/Pt films deposited on MgO. In the insets the contribution of the Cr film only is shown after the subtraction of the Pt cap layer signal. Reprinted with permission from [40]. Copyright (2004) American Chemical Society.

5.6. Magnetic films for high density data storage

In the search for new materials for high density magnetic recording media applications, the chemically ordered nanostructured Co-based ferromagnetic alloys have recently received much interest [83, 84] due to their high anisotropy constant. One of the main requirements for this application is to obtain epitaxial films with good textures, smooth surfaces and very low roughness. Therefore, in [40] the authors used the EDXR technique, in combination with the ED diffraction technique, to investigate double layer Cr/Pt thin films (recently studied for their application as resistors, capacitor plates and in magnetic recording hard disks). The synergy of the two x-ray techniques allowed us to correlate the structural properties and morphological characteristics of the samples, grown by pulsed laser deposition (PLD) at different temperatures on various crystalline and amorphous substrates, with the deposition conditions.

The reflectivity profiles of the samples deposited on the Si and MgO substrates, respectively, are shown in figures 15 and 16 in semilog graphs together with their fits. A minimum thickness (namely of 20 Å) of the Pt cap layer is needed to prevent the oxidation of the Cr film. Its surface is estimated to be atomically flat (namely below 2 Å). The result is a Cr film characterized by a rather low roughness value (less than 6 Å), above which the magnetic properties get too degraded. Since the two layers have different thicknesses, the patterns exhibit a double modulation. The first is due to the interference between the reflections coming from the Pt surface and from the Pt/Cr interface. The second is due to the interference between the reflections from the Pt/Cr and the Cr/substrate interfaces. Since only half of the first oscillation due to the cap layer thinness is visible, the thickness of the Pt layer was estimated by a Gaussian fit of this broad hunch. On the contrary, the Cr thickness (d) has been calculated by the simplified formula valid for large q values: $d = \Delta q/2\pi$.

The Pt film contribution to the signal was subtracted to evaluate oscillation dumping related to the Cr film roughness. An interesting feature of the ED reflectometry lies in the fact that it is a spectroscopy-based technique. Therefore, it also allows the detection of the presence of chemical impurities that may contaminate the films, though the detection of the characteristic fluorescence lines or absorption threshold of the extraneous elements should be visible in the patterns. Actually, in the present case, the reflection pattern of one of the films shows the fluorescence lines and the absorption edge of the Ag contaminant, coming from the silver-print. In fact, the EDXD characterization confirmed that the epitaxy of this particular film was degraded.

The investigation was extended to the study of other magnetic films, namely, the double layer CoPt/Cr thin films deposited by PLD on MgO (100) in [41]. Film roughness is a crucial information for magneto-recording applications, which must be as low as possible. The EDXR systematic study in [41] showed that the CoPt layer, having a film thickness ranging between 43 and 145 Å, is always characterized by an atomically flat roughness at lower deposition temperatures (below 100 °C). The roughness value increases with temperature up to a maximum value of 22 ± 4 Å, well below the limit required (50 Å), when the deposition temperature exceeds 200 °C.

5.7. Organic solar cells

The EDXR technique allowed a major problem in organic PV cell technology to be addressed, namely device degradation [85]. The system stability, both under storage conditions and when exposed to sunlight, was investigated [42]. The bulk heterojunction solar cells used in this study consisted of a multilayered system using an organic film (MDMO − PPV + PCBM) as an active layer between the transparent ITO electrode deposited on a glass substrate and the Al electrode. The technique was used to study the morphology of the device at the electrode–active layer interface for the first time. As previously discussed, the x-ray reflectivity patterns of multilayered samples are composed of the superposition of the signals coming from the various interfaces. In the present case, in order to identify each contribution to the overall
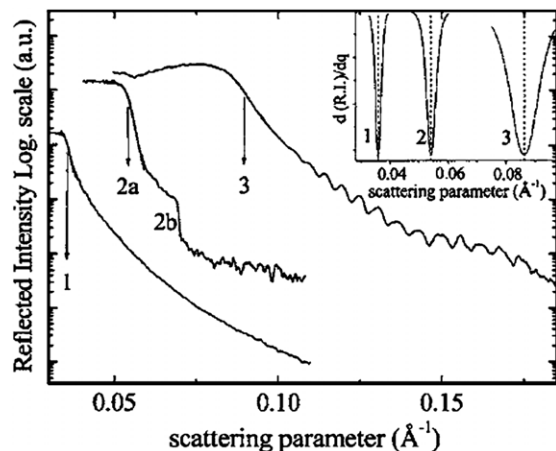
Figure 17. EDXR patterns collected upon three different layered systems, as a function of the scattering parameter. In the inset, the derivatives of the reflectivity edge fits are calculated to deduce the critical parameter. Reprinted with permission from [42]. Copyright (2005), American Institute of Physics.
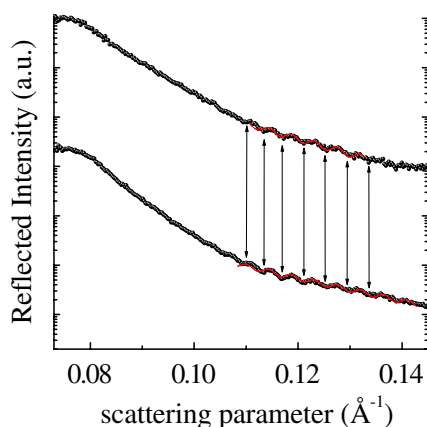

Figure 18. Reflectivity spectra collected at a time distance of several months are plotted as a function of the scattering parameter. The arrows connecting the oscillations minima stress that no morphological change has occurred. Reprinted with permission from [42]. Copyright (2005), American Institute of Physics.

signal, samples corresponding to subsequent stages of the cell construction were measured independently.

The results are reported in figure 17 and they correspond, respectively, to (1) glass/ ITO/ MDMO − PPV + PCBM, (2) glass/ ITO and (3) glass/ ITO/ MDMO − PPV + PCBM/Al. The scattering length densities of each layer were evaluated by individuating the critical edges of the x-ray reflectivity profiles that, in turn, were obtained by processing the derivative of the reflection profile fit (inset of figure 17).

Furthermore, the morphological stability of the device under ambient condition was verified by *ex situ* EDXR measurements (see figure 18). The measurements repeated at a distance of some months demonstrated that the morphology of the device does not change if the cell is stored in the dark under ambient conditions, even for long periods of time.

The situation changes when the same system is studied by *in situ* EDXR measurements, performed under controlled atmospheric conditions and upon illumination (see section 6.2).
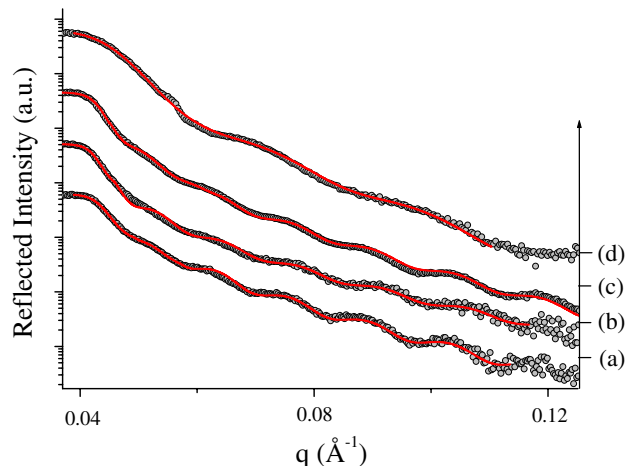
Figure 19. EDXR spectra on (*a*) $Ge/Mn_{0.04}GE_{0.96}$ sample grown at 523 K and $Ge/Mn_{0.02}GE_{0.98}/Ge$ for samples grown at (*b*) RT, (*c*) 423 K and (*d*) 523 K. The continuous lines are the fits according the Parratt model.

5.8. Eterojunctions (GeMn on Ge)

EDXR was applied together with other techniques (reflection high energy electron diffraction and magneto-optical Kerr spectroscopy) to investigate the structural and magnetic properties of $Ge/Mn_xGE_{1-x}/Ge(001)2x1$ magnetic semiconductor [43]. The films studied, deposited by molecular beam epitaxy (MBE) on Ge(001) substrates, showed an epitaxial growth that was investigated *ex situ* by EDXR. The technique allowed the retrieval of information on the films average thickness, the films roughness and the Ge and Mn electronic density.

A selection of the EDXR patterns and fits are shown in figure 19. In particular, in the case of the two films grown at the same temperature (523° K) but with different Mn contributions, the ratio between the $Ge/GE_{0.98}Mn_{0.02}/Ge(001)$ film (pattern d) and the $Ge/GE_{0.96}Mn_{0.04}/Ge(001)$ film (pattern a) electron densities was deduced. The result confirmed what was expected on the base of the deposition parameters.

This investigation can be considered as a test of the high sensitivity of the EDXR measurements to the electronic density of the materials, allowing differences of SLD induced by very small Mn concentration variations to be detected.

6. Further application: *In situ* time-resolved EDXR

6.1. Study of the interaction between gas and gas sensor films

As mentioned above, phthalocyanine film morphology plays a fundamental role in the film's electrical response to gas exposure, from the point of view of both the charge transfer and the carrier transport. For this reason the metal phthalocyanines–NO_2 gas interaction was extensively studied by using EDXR [37, 44–46].

In particular, the $Ti(Pc)_2$ system was systematically studied [45] to validate the theoretical models attributing the change in electrical conductivity to a diffusion of the NO_2 molecules in the film's bulk. Indeed, the *in situ* real time EDXR characterization of the morphological changes upon different films during exposure to a 50 ppm gas concentration revealed a 'breathing like' expansion of the $Ti(Pc)_2$ matrix. In figure 20, a
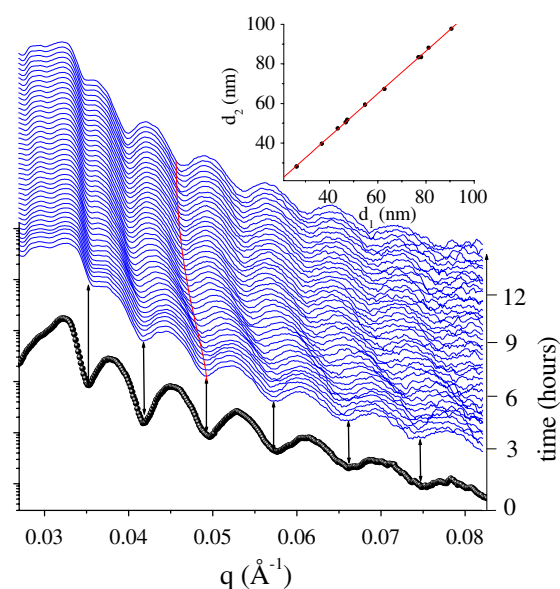
Figure 20. Sequences of time-resolved EDXR spectra for a 80 nm TiPc$_2$ film exposed to an NO$_2$ gas flux of 20 nmol s^{-1}. The arrow connecting the minima of the second oscillation evidences the phase shift. Reprinted with permission from [45]. Copyright (2005), American Institute of Physics.

sequence of reflectivity patterns collected every 15 min during the overall NO$_2$ exposure time is shown.

The shift of the Kiessig fringes towards lower q values is indicative of a thickening of the film. After accurate data processing, the kinetic behaviour of the parameters d and σ was obtained, as shown in figure 21.

The authors compared this behaviour with that shown by other MPcs, (M=Cu and Pb, respectively) and in all cases the evolution of this morphological parameter is perfectly consistent with a one-step bulk diffusion. Moreover, the EDXR technique did not only confirm the theoretical models proposed to describe the gas–film interaction but added some novel information, since the evolution of the roughness parameter showed some unexpected behaviour. Indeed, an increase in the surface roughness value is expected because of the interaction of the NO$_2$ molecules on the Pc's surfaces but, during the subsequent diffusion of the gas molecules in the bulk, the Ti(Pc)$_2$ film surface behaves in an unpredictable way. As shown in figure 21 (2b), the Ti(Pc)$_2$ $\sigma(t)$ curve exhibits a peak, i.e. after a normal initial rise up to a maximum value, it begins to decrease until a final constant value is reached.

This final value is comparable to the initial one or only slightly higher. The authors made two different hypotheses to explain this behaviour: it might be either due to a kinetic effect (crowding of molecules onto the surface) or to a thermodynamic effect (surface structure rearrangement). To discriminate between the two possibilities, further time-resolved *in situ* EDXR measurements were performed at different NO$_2$ concentrations. These measurements showed that the surface roughness behaviour is independent of the NO$_2$ concentration: the only effect of a lower concentration was to slow down the process. In conclusion, the EDXR experiments performed on the NO$_2$ sensing device Ti(Pc)$_2$ not only validated the theoretic hypothesis that diffusion occurs in the film's bulk but were able to describe the dynamics of the
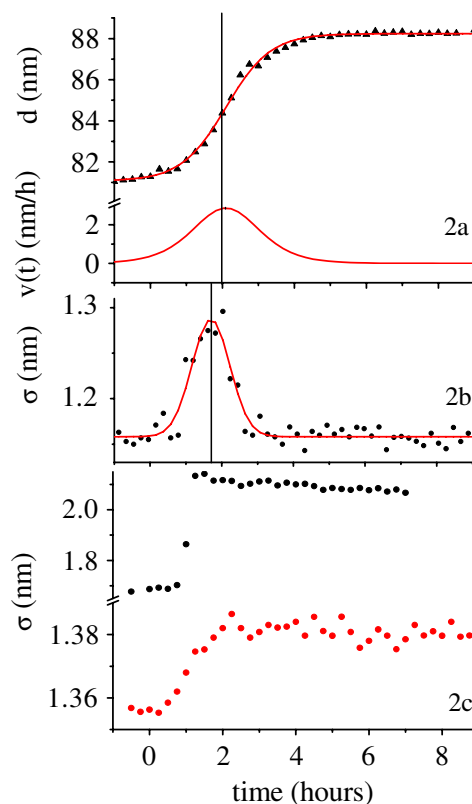
Figure 21. (2a) The thickness time evolution of an 80 nm nominally thick TiPc$_2$ film is shown with its derivative. The process is well fitted by a Boltzmann growth. In (2b) the time evolution of the roughness σ of the same sample is plotted and in (2c) the evolution of the same parameter is shown in the case of a PbPc and a CuPc film, respectively. Reprinted with permission from [45]. Copyright (2005), American Institute of Physics.

mechanism taking place. Moreover, for the first time, evidence of a surface structural rearrangement in a MPc was shown.

The same method was applied to investigate also the (RuPc)$_2$ system, in order to explore its potentialities as a NO$_2$ sensing device, this system being an intrinsic semiconductor.

In [44] the morphological response of thin (RuPc)$_2$ films was monitored *in situ* during the exposure of the material to the pollutant NO$_2$ 50 ppm gas flux.

The fitting procedure of the reflectivity pattern sequences revealed an anomalous behaviour of the parameter thickness during the gas–film interaction. As visible in figure 22, these MPc films did not exhibit a simple bulk expansion, as Ti(Pc)$_2$ did. Indeed, the thickness parameter undergoes a two-step evolution: initially, a fast growth occurs as the gas comes into contact with the film's surface, whose characteristic time response corresponds to that of the surface roughness increase and is independent of the film's thickness.

Subsequently, a second process takes place, which corresponds to a slower increase in thickness and whose time response is dependent on the film's initial thickness. The intermediate point between the two processes corresponds to a visible discontinuity in the evolution of the thickness parameter. This first evidence of a two step gas–film interaction was investigated in [46]. A systematic EDXR study proves that these two behaviours are related to surface absorption and bulk diffusion, respectively.
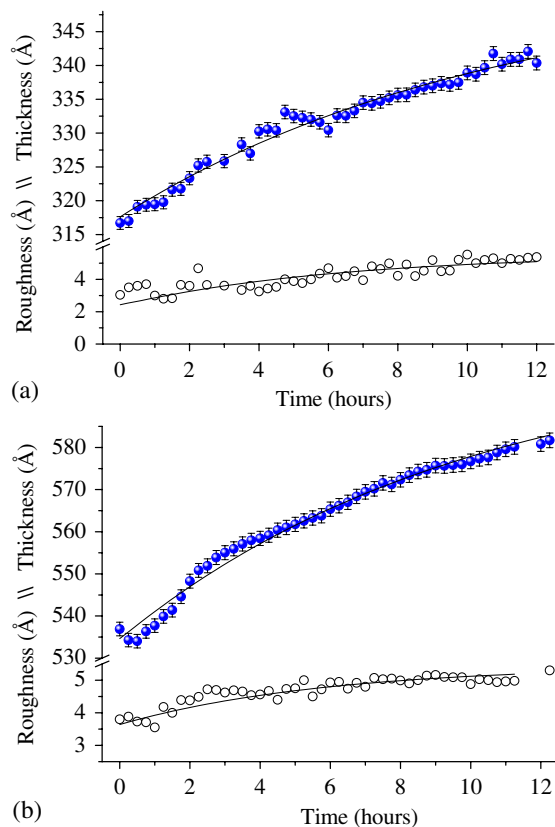
Figure 22. Curves of the $(RuPc)_2$ films thickness (full dots) and roughness (open dots) as a function of time, obtained by the Parratt's model, for the 300 Å (a) and 500 Å (b) films, respectively. The solid line represents the fit of the data points. Reprinted with permission from [44]. Copyright (2003), American Institute of Physics.

Further investigations provided more information on the potentialities of $(RuPc)_2$ as a sensing device, testing the films capability of being reset and reconfirming the interaction mechanism model. When thermally treated, these materials should release the gas molecules entrapped in their bulk and be able to act again as sensing devices upon successive exposures (reset).

In figures 23 and 24 two examples are reported. In parts (a), (b) and (c), the evolution of the thickness, the roughness and the reflectivity spectra corresponding to the initial (d_1, σ_1), the intermediate (d^*, σ^*) and the final morphology (d_2, σ_2) are shown. In figures 23(d) and 24(d), the reflectivity spectra collected after a $130\,^\circ\text{C}$ 30 min thermal treatment and the pattern obtained after a $200\,^\circ\text{C}$ 30 min thermal treatment, respectively, are shown. What is clearly visible is that after a $130\,^\circ\text{C}$ treatment a partial recovery is obtained, i.e. the intermediate (transition) morphology is regained. In the other case, when the sample is exposed to a temperature of $200\,^\circ\text{C}$, a complete morphological recovery is obtained.

This evidence reconfirms the two-step mechanism, revealing further information on the chemical nature of the interactions and discriminating the energies of the two processes. Another interesting characteristic is that, after the films had been thermally treated, their efficiency towards NO_2 molecules (when re-exposed to the same gas flux during a second cycle) appeared to be enhanced as shown in figure 25. In this case, only bulk diffusion is present.
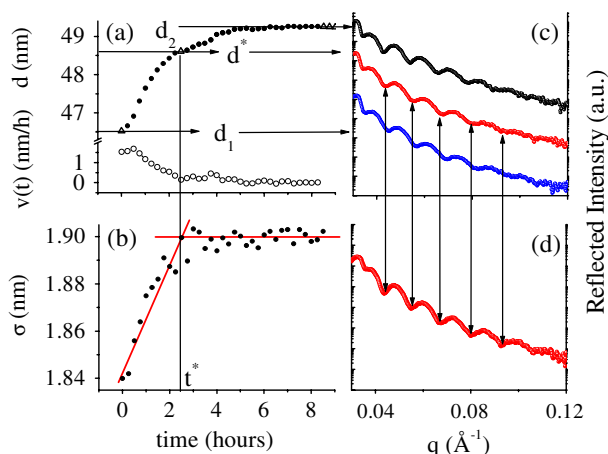
Figure 23. (a) Time dependence of the $(RuPc)_2$ layer thickness d (full dots) and its derivative $v(t)$ (open dots), for sample-1. (b) Time dependence of the $(RuPc)_2$ layer roughness σ (full dots). (c) Reflectivity profiles relative to the d_2, d^* and the d_1 values recorded *in situ*. (d) The bottom spectrum is recorded *ex situ* after heat treatment of the same sample at $T = 130\,^\circ$. Reprinted with permission from [46]. Copyright (2005), American Institute of Physics.
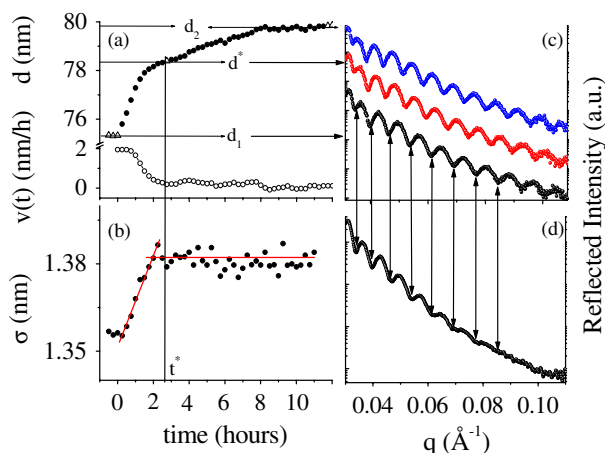
Figure 24. (a) Time dependence of the $(RuPc)_2$ layer thickness d (full dots) and its derivative $v(t)$ (open dots), for sample-2. (b) Time dependence of the $(RuPc)_2$ layer roughness σ (full dots). (c) Reflectivity profiles relative to the d_2, d^* and the d_1 values recorded *in situ*. (d) The bottom spectrum is recorded *ex situ* after heat treatment of the same sample at $T = 200\,^\circ$. Reprinted with permission from [46]. Copyright (2005), American Institute of Physics.

Thus, *in situ* EDXR proved to be a powerful tool to study and distinguish the gas–film interaction mechanisms, a fundamental aspect in developing novel gas sensing devices.

6.2. Organic solar cells upon working

In the engineering of organic electronic devices the interface between the conducting polymer (or another organic material) and the metallic contact is the most critical part. In [42], the authors have applied *in situ* ED x-ray reflectometry to study this interface on working solar cells and associated the deterioration of the device with a change at this interface.

Such a study is the first example reported in the literature of time-resolved investigation of the morphological changes
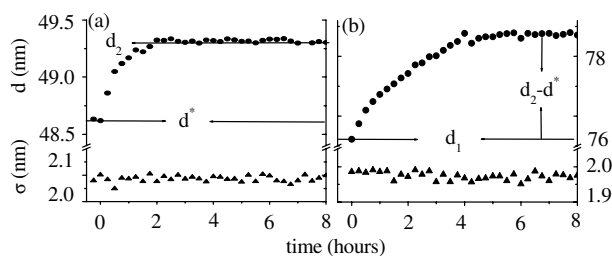
Figure 25. Time dependence of the (RuPc)$_2$ layer thickness (full dots) and roughness (triangles) at the second submission to the gas. (*a*) The thickness of sample-1 increases from d^* to d_2. (*b*) The thickness of sample-2 increases from d_1 to $(d_1 + d_2 - \tilde{d}^*)$. The roughness does not show any significant increase. Reprinted with permission from [46]. Copyright (2005), American Institute of Physics.
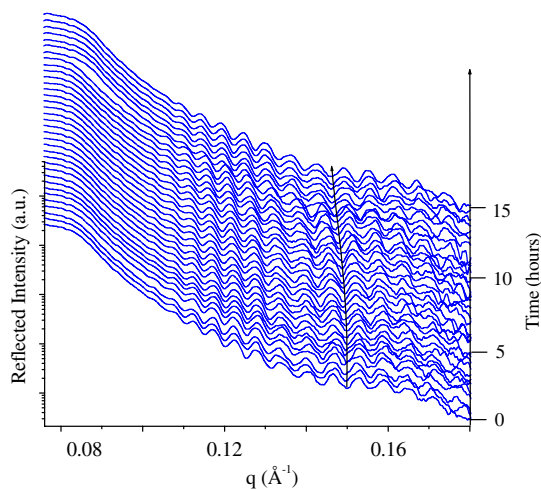
Figure 26. Sequence of EDXR patterns collected as a function of the scattering parameter and time. The arrow shows the shift towards lower q values of the oscillations, indicating that a thickening is taking place. Reprinted with permission from [42]. Copyright (2005), American Institute of Physics.

experienced by an organic electronic device upon working conditions.

The device was exposed to artificial light for 15 h, during which the changes in the system morphology at the electrode–active layer interface were monitored (see figure 26).

A progressive thickening of the Al film was observed, which appears to be in two steps. Indeed two Boltzman sigmoids had to be used in the fit of the Al film thickness versus time curve, as reported in figure 27.

This two-step process occurring at the Al electrode–active layer interface, which was detected owing to the high statistical accuracy of the data, was correlated with a photo-oxidation of the Al electrode and associated with the reduction in the performances of the device. The results [42] therefore validated the use of the EDXR technique applied *in situ* as a powerful non-destructive tool to investigate the ageing effects of the different layers of polymer PV devices in working conditions.

6.3. Humidity sensors

Mesoporous metal oxide thin films with highly ordered pores and a large specific area are potential humidity sensing devices.
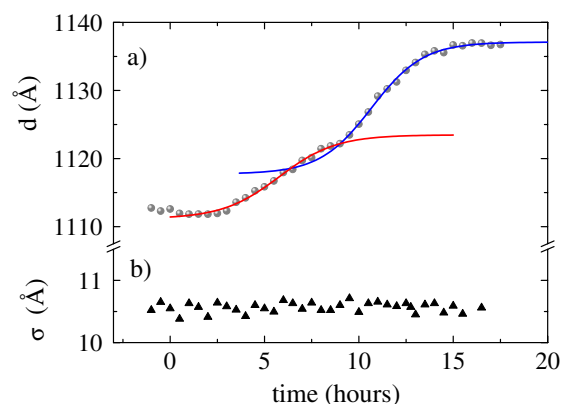
Figure 27. Time evolution of thickness (*d*) and roughness (σ) of the Al electrode, obtained by the Parratt fitting procedure of the EDXR patterns. The thickness evolution is well fitted by two Boltzmann curves indicating a two-step process. The second process starts when the first is almost concluded. Reprinted with permission from [42]. Copyright (2005), American Institute of Physics.

The performances of such sensors were found to be dependent on the film preparation method, especially on the calcination temperature and on its duration, since thermal treatments modify the pore structure. Therefore, it was possible to show that the structural changes of the sensing material play a role in the electrical response modifications observed in testing experiments. In mentioned previously [39], preliminary *ex situ* EDXR measurements allowed the pore dimensions and the internal order of Si mesoporous thin films, as a function of the calcinating temperature, to be measured.

Among such films the one calcinated at 950 °C still showed the presence of an internal structure, even though the reflection intensity was very weak and the Bragg peak became extremely broad (see figure 14, section 5.5). In this case the sample still retains a certain degree of order at high calcination temperature. A test was therefore performed in order to investigate the stability of its internal structure changing the ambient conditions.

The sample was first exposed to a controlled N$_2$ flux (180 nmol s^{-1}), then to room atmosphere and finally to controlled N$_2$ flux again. The residence time in such conditions was 12 h for each phase. During the overall 36 h, the sample was irradiated by an x-ray beam at grazing incidence and a sequence of 15 min long x-ray reflectivity spectra was collected *in situ* (see figure 28).

As shown in figure 28, passing from the N$_2$ gas flux to room atmosphere (and back), no variation was observed in the collected spectra: the Bragg peak position remains unchanged and so does its shape. Furthermore, the slope of the underlying reflectivity profile is constant. The arrows connecting the first to the last patterns underlines the reproducibility of the reflectivity patterns shapes.

This was evidence that no morphological modifications occurred. Indeed, the film morphology is stable in air, and this is a fundamental condition when processing humidity sensing devices.

6.4. in situ structural changes in thin films

6.4.1. Film growth. Traditionally, structural and morphological sample characterization is performed after

deposition and in many situations this procedure is fully consistent. In particular cases, however, such as the deposition of multilayers, obtaining detailed information on-line (namely, during the layer deposition) would be extremely important for performing corrections and optimizing the coating parameters. Such information is particularly useful when the materials are precious and a deposition failure would be expensive. *in situ* time-resolved x-ray reflectivity measurements are still rarely used for monitoring complex growth processes, but some experimental apparata have been optimized for this purpose. Malaurent *et al* [47] first used this technique to monitor *in situ* multilayers growth, providing their reflectometers (a Spiller-type reflectometer and an ED reflectometer equipped with an Ag anode tube and a Si(Li) single crystal solid state detector) with the coating system.

They tested this new method by observing the growth of a 5 nm period Mo/Si multilayer (about 2 nm Mo and 3 nm Si) onto float glass using electron beam evaporation in one case
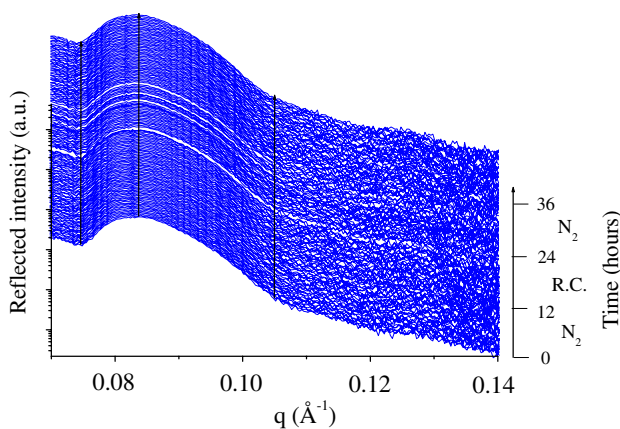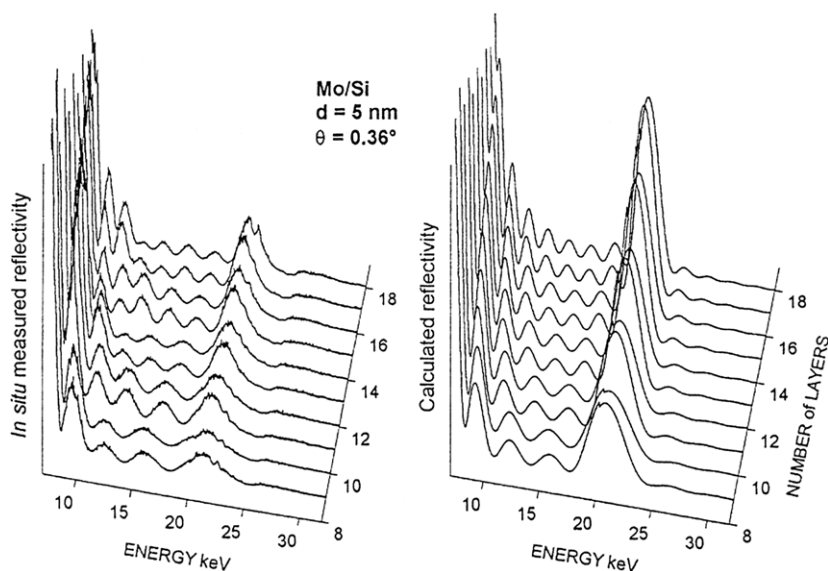
and sputtering in another. A relatively high reflection angle was fixed (0.36° and 0.48°, respectively) in order to explore a wide q range. The energy window was set between 5 and 30 keV. In figure 29, on the left side, the reflectivity patterns recorded after the deposition of each Mo/Si couple of layers (from layer 9 to layer 18), with a time resolution of 230 s, are shown. The spectra present both Kiessig fringes and the first Bragg superlattice peak. The former signal increases in frequency by increasing the number of layers deposited, until the total multilayer thickness becomes too elevated, giving rise to oscillations whose energy width becomes smaller than the detector's energy resolution (see figure 30).

The Bragg peak, instead, is characterized by an increasing intensity as the deposition goes on, saturating to a maximum intensity value when the number of deposited layers exceeds a certain threshold (ca 70 layers).

In the right side of figure 29, the simulated results, assuming ideal multilayers and perfectly sharp interfaces, are shown. An important advantage of EDXR on the AD counterpart, when multilayers are concerned, is that the former allows us to observe directly the amount of the possible contribution of higher order harmonics to the reflected signal and this can be done even during the deposition. To illustrate this kind of monitoring, a novel 9.23 nm thick period Mo/Si multilayer with 2.5 nm thick Mo layers was deposited by sputtering.

In order to evaluate the kinetic evolution of the Bragg peaks produced by the harmonics, a higher incidence angle was chosen to explore a wider q range ($\theta = 0.55°$).

In figure 30, the reflectivity spectra collected after the deposition of 19, 29 and 99 layers, respectively, are compared. The first Bragg peak remains constant both in intensity (saturated before the 19th layer was deposited) and position, while the others progressively saturate and shift towards lower energies. This is probably due to a slight variation in the incidence angle during deposition rather than to an increase in the layer thickness.

Figure 28. Sequence of reflectivity patterns collected as a function of the scattering parameter. The counting rate of each spectrum corresponds to 15 min, the whole collection enduring 36 h in alternate atmospheres: (*a*), (*c*) N_2 gas flux; (*b*) room conditions.

Figure 29. EDXR patterns, collected during the growth of a Mo/Si multilayer, are shown (left side) as a function of the x-ray energy. On the right side, the simulated reflectivity curves are plotted for comparison. Reprinted from [47]. Copyright (2000), with permission from Elsevier.
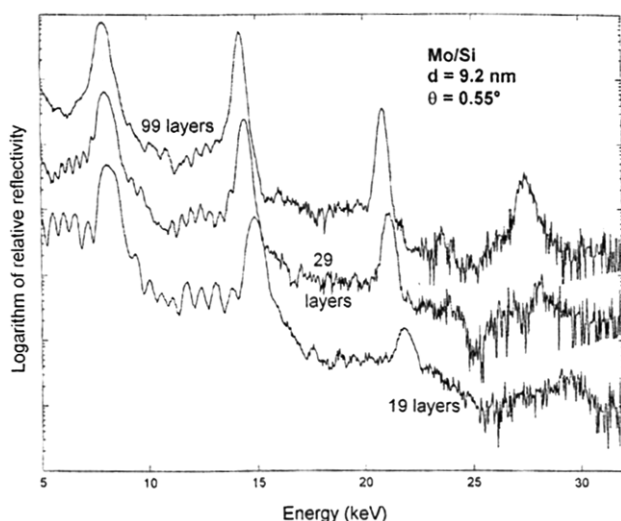
Figure 30. Reflectivity profiles of a Mo/Si multilayer are collected as a function of the x-ray energy and of the number of layers deposited. As the layer gets thicker, a shift in the Bragg signals towards lower energies is visible. Reprinted from [47]. Copyright (2000), with permission from Elsevier.

In conclusion, *in situ* x-ray reflectivity proved to be very useful for monitoring the multilayer deposition in real time, especially when multilayers for x-rays optics are to be prepared. However, if the sample period is not uniform, the divergence of the beam can induce possible systematic errors.

An x-ray configuration similar to that described above was used by Summers *et al* [48] to grow films of tantalum on silicon wafers with different growing rates. The deposition was performed by evaporation and the surface roughness was found to increase with the deposition rate. Moreover, a computational model was developed to evaluate the evolution of thickness, density and roughness for thin films as a function of the deposition rate and the results were in accordance with other models that are reported in the literature for evaporated and sputtered films.

6.4.2. Film annealing. Thin films and multilayers made up of organic materials and metals are often the basis for devices of technological interest. The optimization of such devices and the investigation of their performances are related to their morphology for many reasons (variations at the interfaces, diffusion between different layers, etc). Orita *et al* [49] first applied this technique to monitor organic electroluminescent films during annealing processes. In fact, despite the widespread use of such devices, the reasons for their deterioration, somehow connected to the structural changes occurring during the annealing process, are not clear.

Typical organic material were selected in order to deposit films on Si wafer substrates with good surface smoothness. N, N'-diphenyl-N, N'-bis(3-methylphenyl)-(1,1′-biphenyl)-4,4′diamine (TPD) and Alq$_3$/TPD were deposited by vacuum sublimation obtaining 150 and 300 Å thick films, respectively.

To perform the EDXR measurements, incident white x-rays produced by a rotating Mo anode (60 kV and 10–200 mA) were collimated by a four slit system and finally collected by a pure Ge single crystal detector. Atomic force microscopy
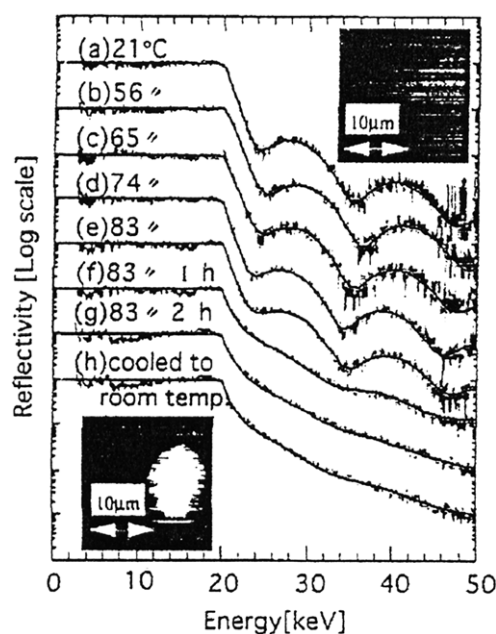
Figure 31. Sequence of reflectivity patterns as a function of the x-ray energy, collected upon TPD/Si films at various times. Solid lines are the theoretical curves fitting the experimental data. In the upper right corner and the left bottom corner, AFM images show the sample morphology before and after the thermal treatment. Reprinted from [49]. Copyright (1997), with permission from Elsevier.

(AFM) was also used to observe the surface morphology and compare the roughness data obtained in this way with the information derived from x-ray analysis.

The two different thin films (TPD and Alq$_3$/TPD) were annealed at 83 °C and 74 °C, respectively.

In both cases, the EDXR patterns were collected every 1000 s during the heating of the samples. After the annealing temperature was reached, the collection was performed with a time resolution of 1 h for each TPD reflectivity pattern and 0.5 h for the Alq$_3$/TPD spectra. During the heating process, no morphological modification occurred on both samples, i.e. the reflectivity patterns were perfectly reproduced. When the final annealing temperatures were reached, the reflectivity patterns appeared to be visibly modified, i.e. the oscillations dramatically damped until the fringes were no longer visible.

Figure 31 shows the modifications in the x-ray reflectivity profiles of TPD films upon Si wafers, observed during the annealing up to 83 °C, together with the calculated patterns (straight lines). The insets are AFM images showing the TPD topography before (upper) and after (lower) annealing.

By the fitting procedure, the authors state that after 1 h at 83 °C, the TPD films thickness increases by 1 nm while its density decreases by ca 0.1 g cm^{-3}, suggesting that TPD film structures are unstable even at such low temperatures. In fact, the AFM images confirm that a structural modification has occurred in the film, since discontinuous areas with islands (20–90 nm height) are present.

With regard to Alq$_3$/TPD, the instability of the TPD film affects that of Alq$_3$. Indeed, despite the fact that Alq$_3$ is a stable material when the above-mentioned temperatures are concerned, the reflectivity patterns in the multilayer show a decrease in thickness associated with the mutual diffusion
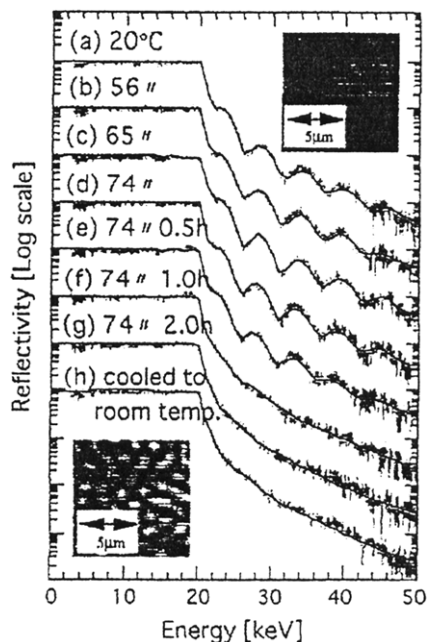
Figure 32. Sequence of reflectivity patterns as a function of the x-ray energy, collected upon the Alq₃/TPD/Si film at various temperatures. Solid lines are the theoretical curves fitting the experimental data. In the upper right corner and the left bottom corner, AFM images show the sample morphology before and after the thermal treatment. Reprinted from [49]. Copyright (1997), with permission from Elsevier.

of the two materials. Figure 32 shows the changes in the reflectivity profiles of the Alq₃/TPD/Si and AFM images of the film before and after the annealing process.

Due to the little difference between the refractive indexes of Alq₃ and TPD layers, their interface roughness could not be clearly evaluated. However, after 1 h at 74 °C, the Kiessig fringes disappear revealing that the roughness of Alq₃ has increased above 6.0 nm in that time. In fact the lower AFM image, collected after the annealing process, confirms a surface roughness of about 10.0 nm.

6.5. Surface corrosion and growth of oxides on clean surfaces

In situ time-resolved energy dispersive x-ray reflectivity technique proved to be suitable also for studying the oxidation processes on the nanometre scale, even in the most complicated case, i.e. the oxidation of liquid metals.

Indeed, the study of oxidation processes is a well-established field in material research due to its importance in corrosion phenomena (metallurgy) and in semiconductor technology. Many theoretical models have been proposed for the growth of oxide layers up to now, e.g. the well-known parabolic law [86] and logarithmic and inverse-logarithmic laws [87,88]. However, very little experimental data are available on the oxidation kinetics of metals due to experimental difficulties. The EDXR technique turns out to be especially suitable for investigating time-dependant phenomena and liquids, because of the fast data collection at high momentum transfer without moving the sample. The EDXR was used in this case to investigate the low temperature oxidation kinetics of liquid Ga and of the liquid Ga₀.₉₃Hg₀.₀₇ alloy [50].
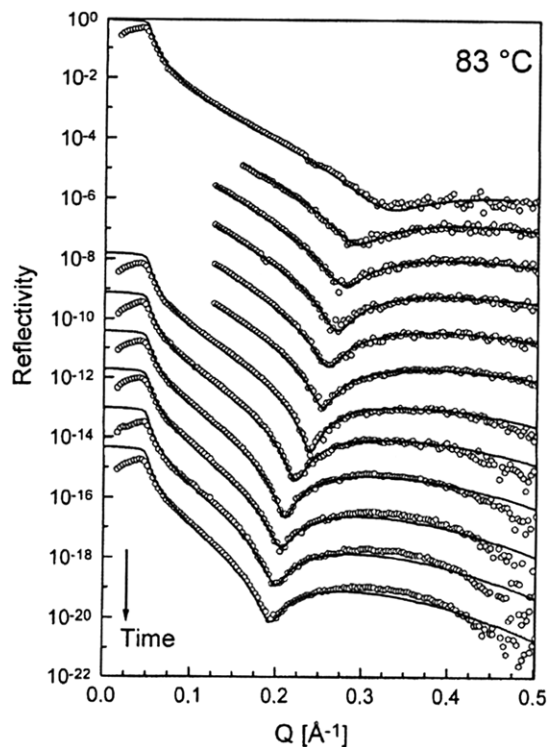
Figure 33. Reflectivity patterns (dots) collected during the oxidation of Ga₀.₉₃Hg₀.₀₇. The spectra at the top show the data obtained at room temperature while the lower ones refer to successive times after rapid heating $T = 83$ °C. The Parratt fits to the data are represented by solid lines. Reprinted from [50]. Copyright (1998) IOP Publishing Ltd.

The reflectometer consisted of a 3 kW molybdenum tube operating at 50 kV, collimating slits and a sample holder allowing vertical motion in order to select a reflection angle. A nitrogen-cooled Ge single crystal detector, with a resolution of 200–300 eV at energies between 5–45 keV, was used. Three different temperatures were chosen to monitor the oxidative process (83 °C, 107.5 °C and 122 °C, respectively). The samples were either high purity Ga or mixtures of high purity Ga and Hg. Several alloys were prepared by changing the Ga/Hg proportion and studied at each oxidation temperature to check the consistency of the results.

The liquid alloys were inserted into a stainless steel trough within a furnace chamber at ambient conditions. Very thick layers (400 μm) were prepared in order to suppress mechanically excited low-frequency surface waves and curvature effects on the liquid sample. Moreover, after inserting the samples, the pre-existing oxide layer was removed in order to measure the clean surface before the oxidative mechanism started.

In figure 33, an example of a reflectivity sequence is shown in the case of oxide growth at 83 °C on the Ga₀.₉₃Hg₀.₀₇ liquid surface.

The patterns are reported as a function of the scattering parameter and with a time resolution equal to 20 min. Starting from the top of figure 33, it is evident even by the naked eye that, as time passes, the oscillations of the reflectivity profiles shift towards lower q values, i.e. the oxide layer on the liquid surface becomes thicker. The overall growth of the oxide layer
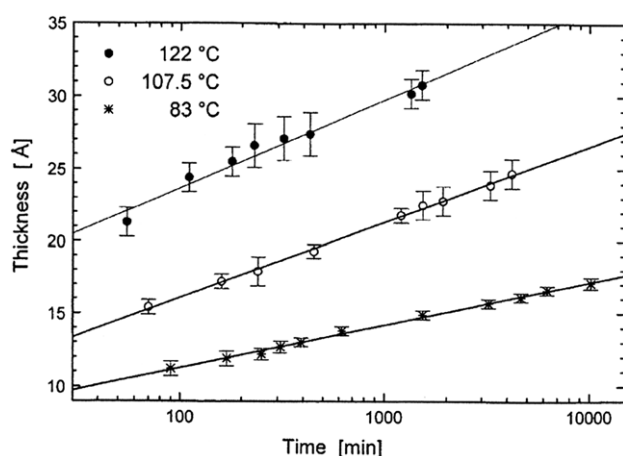
Figure 34. Thickness of the oxide layer on $Ga_{0.93}Hg_{0.07}$ as a function of time. Each solid line represents a straight-line fit. Reprinted from [50]. Copyright (1998) IOP Publishing Ltd.

has been monitored for 5 h. Furthermore, every reflectivity pattern has been fitted to obtain an independent determination of the surface roughness and thickness. As visible in figure 33 (solid lines), the reflectivity data are well reproduced by the fits, assuming that a single oxide layer with constant density (single box model) is formed, and with a thickness ranging from 8 to 12 Å, depending on the sample investigated. The surface and interface roughness (RMS) changes slightly during the oxidation process, remaining within the value range 4–6 Å for all fits.

The chemical composition of the oxide was assumed to be Ga_2O_3 (for both alloys) since this is the oxide which naturally forms from liquid Ga in air. The density of these thin layers was determined ($3.4 \pm 0.2\,\mathrm{g\,cm^{-3}}$). It is constant and equal to the value of the density of the layer present at room temperature.

This experimental procedure has been applied to all samples at the various temperatures, and the time evolution of the surface morphology has been monitored. Finally, in figure 34, the growth of the oxide layer (its thickness) is shown as a function of time at the three different temperatures.

It is worth noting that the EDXR technique is well suited for monitoring the growth of even very thin oxide layers, as a function of time and of the oxidation temperature. A logarithmic law was found for the oxidation of liquid $Ga_{0.93}Hg_{0.07}$, demonstrating also that this is the actual behaviour of ultra-thin films (below 4 nm). As expected for a temperature-activated oxidation process, the oxide thickness increases with temperature, resulting in layers ranging from 20 to 30 Å at 122 °C compared with 12–17 Å at 83 °C.

This first example of applications to monitor the growth of oxides on liquid surfaces indicates that the *in situ* time-resolved EDXR is promising for studying general oxidation processes, being able to follow fast growth kinetics. Further optimization of the experimental setup must first be achieved, however.

6.6. Real time structural study of light elements films

The EDXR technique has been used *in situ* [51], along with the multiple beam optical stress (MOSS) technique (suitable for stress measurements), to study the morphology of amorphous thin boron films grown on silicon substrate. The film roughness

and crystallinity is crucial in the development of new structural materials based on light elements films and coatings and the possibility to monitor such parameters in real time is an important tool. The EDXR is particularly suitable to study light elements films, since the reflected intensity depends on the density differences between film and substrate rather than on the scattering power of the film. In the present experimental setup the EDXR and MOSS measurements were performed simultaneously *in situ* using an ultra-high vacuum chamber for chemical vapour deposition (UHV-CVD) reactor. In this case, the qualities of the ED mode, which allows collecting data in a rapid way and keeping the illuminated part of the sample unchanged, play a key role. The film thickness and roughness were obtained as a function of the deposition time (i.e. after 20 and 40 min of deposition). The results were compared with Rutherford backscattering-based thickness estimations. This work shows the potentialities of the EDXR technique, operating *in situ* during film growth and adaptable to many commercial CVD reactors, for the study of light elements films.

References

[1] Parratt L G 1954 *Phys. Rev.* **95** 359
[2] Richardson R M and Roser S J 1987 *Liq. Cryst.* **2** 797–814
[3] Grundy M J, Richardson R M, Roser S J, Penfold J and Ward R C 1988 *Thin Solid Films* **159** 43–52
[4] Pluis B, Gay J M, Frenken J W M, Gierlotka S and Van Der Veen J F 1989 *Surf. Sci.* **222** L845–52
[5] Dietrich S and Haase A 1995 *Phys. Rep.* **260** 1
[6] Felici R 1993 *Acta Phys.-Pol.* A **84** 193-202
[7] Sinha S K 1991 *Physica* B **173** 25
[8] Als-Nielsen J, Christensen F and Pershan P S 1982 *Phys. Rev. Lett.* **48** 1107
[9] Dietrich S and Schack R 1987 *Phys. Rev. Lett.* **58** 140
[10] Bhattacharya M, Mukherjee M and Sanyal M K 2003 *J. Appl. Phys.* **94** 2882
[11] Malaurent J C, Dhez P and Duval H 1994 *Opt. Commun.* **136** 1–8
[12] Duval H, Malaurent J C, Dhez P and Duval Ph 1997 *Opt. Commun.* **136** 44–51
[13] Neissendorfer F, Pietsch U, Brezesinski G and Mohvald H 1999 *Meas. Sci. Technol.* **10** 354–61
[14] Pietsch U, Grenzer J, Geue Th, Neissendorfer F, Brezesinski G, Symietz F, Mohvald H and Gudat W 2001 *Nucl. Instrum. Methods* A **467** 1077–80
[15] Le Boité M G, Traverse A, Névot L, Pardo B and Corno J 1988 *Nucl. Instrum. Methods* B **29** 653–60
[16] Lee S L, Windover D, Doxbeck M, Nielsen M, Kumar A and Lu-M 2000 *Thin Solid Films* **377** 447–54
[17] Salditt T, Munster C, Lu J, Vogel M, Fenzl W and Souvorov A 1999 *Phys. Rev.* E **60** 7285
[18] Generosi J, Castellano C, Pozzi D, Congiu Castellano A, Felici R, Natali F and Fagneto G 2004 *J. Appl. Phys.* **96** 6839–44
[19] Wang J, Park Y J, Lee K-B, Hong H and Davidov D 2002 *Phys. Rev. B* **66** 161201
[20] Sinha S K, Sirota E B and Garof S 1988 *Phys. Rev. B* **38** 2297
[21] Henke B L, Gallikson E M and Davis J C 1993 *At. Data Nucl. Data Tables* **54** 181
[22] Nevot L and Croce P 1986 *Phys. Rev. Appl.* **15** 711
[23] Gibaud A, Mc Morrow D and Swaddling P P 1995 *Phys. Condens. Matter* **7** 2645
[24] Freitag J M and Clemens B M 2001 *J. Appl. Phys.* **89** 1101
[25] de Bernabé A, Capitan M J, Fischer H E and Pieto C 1998 *J. Appl. Phys.* **84** 1881
[26] Toney M F, Mate M C and Leach A K 2000 *J. Appl. Phys.* **77** 3296

[27] Roser S J, Patel H M, Lovell M R, Muir J E and Mann S 1998 *Chem. Commun.* 829

[28] Gasgnier M and Malaurent J C 1978 *J. Appl. Cryst.* **11** 141

[29] Tamura K and Hosokawa S 1992 *J. Non-Cryst. Solids* **150** 29

[30] Hosokawa S, Matsuoka T and Tamura K 1991 *J. Phys.: Condens. Matter* **3** 4443–57

[31] Metzger H, Luidl C, Pietsch U and Vierl U 1994 *Nucl. Instrum. Methods* A **350** 398

[32] Cicala G, Bruno P, Dragone A, Losacco A M, Sadun C and Generosi A 2005 *Thin Solid Films* **48** 264–9

[33] Bilderback D H and Hubbard S 1982 *Nucl. Instrum. Methods* **195** 85–90

[34] Bilderback D H and Hubbard S 1982 *Nucl. Instrum. Methods* **195** 91–5

[35] Windover D, Banet E, Summers J, Gribbin C, Lu T-M, Kumar A, Bakhru H and Lee S L 2000 *Proc. Int. Conf. on Characterization and Metrology for ULSI Technology (Gaithersburg, Maryland, USA)*

[36] Bhattacharya M, Mukhopadhyay M K, Pal S and Sanyal M K 2004 Energy dispersive x-ray reflectivity to study phase transitions in thin films *Radiat. Phys. Chem.* **70** 611–7

[37] Generosi A, Rossi Albertini V, Rossi G, Pennesi G and Caminiti R 2003 *J. Phys. Chem.* B **107** 575–9

[38] Roser S J, Felici R and Eaglesham A 1994 *Langmuir* **10** 3853–6

[39] Mio Bertolo J, Bearzotti A, Generosi A, Palummo L and Rossi Albertini V 2005 *Sensors Actuators* B **111–2** 145

[40] Paci B, Generosi A, Rossi Albertini V, Agostinelli E, Varvaro G and Fiorani D 2004 *Chem. Mater.* **16** 292–8

[41] Paci B, Generosi A, Rossi Albertini V, Agostinelli E and Varvaro G 2004 *J. Magn. Magn. Mater.* **272–276** E873–4

[42] Paci B, Generosi A, Rossi Albertini V, Perfetti P, de Bettignies R, Firon M, Leroy J and Sentein C 2005 *Appl. Phy. Lett.* **87** 194110

[43] De Padova P *et al* 2006 *Surf. Sci.* at press

[44] Rossi Albertini V, Generosi A, Paci B, Perfetti P, Rossi G, Capobianchi A, Paoletti A M and Caminiti R 2003 *Appl. Phys. Lett.* **82** 3868–70

[45] Generosi A, Paci B, Rossi Albertini V, Perfetti P, Paoletti A M, Pennesi G, Rossi G and Caminiti R 2005 *Appl. Phys. Lett.* **87** 181904

[46] Generosi A, Paci B, Rossi Albertini V, Perfetti P, Pennesi G, Paoletti A M, Rossi G, Capobianchi A and Caminiti R 2005 *Appl. Phys. Lett.* **86** 114106

[47] Malaurent J C, Duval H, Chauvineau J P, Hainaut O and Raynal A 2000 In situ x-ray multilayer reflectometry based on the energy dispersive method *Opt. Commun.* **173** 255–63

[48] Summers J, Lu T-M, Windover D and Lee S 2001 *Technical Report* ARCCB-TR-01015, US Army Armament Research

[49] Orita K, Morimura T, Horiuchi T and Matsushige K 1997 In-situ energy-dispersive x-ray reflectivity measurements of structural changes in thin films for organic electroluminescent devices *Synth. Met.* **91** 155–8

[50] Plech A, Klemradt U, Metzger H and Peisl J 1998 *J. Phys.: Condens. Matter* **10** 971–82

[51] Nesting C D, Kouvetakis J, Hearne S, Chason E and Tsong I S T 1999 *J. Vac. Sci. Technol.* A **17** 891

[52] Lekner J 1987 *Theory of Reflection* (Nijhoff Publ.: Dordrechet, The Netherlands)

[53] Born M and Wolf E 1970 *Principles of Optics* (Oxford: Pergamon)

[54] Zhou X L and Chen S H 1995 *Phys. Rep.* **257** 223–348

[55] James R W 1982 *The Optical Principles of the Diffraction of X-rays* (London: Bell)

[56] Tolan M 1999 *X-Ray Scattering from Soft-Matter Thin Films (Springer Tracts in Modern Physics)* (Berlin: Springer)

[57] Compton A H 1923 *Phil. Mag.* **45** 112

[58] Compton A H and Allison S K 1935 *X-rays in Theory and Experiment* (New York: Van Nostrand Reinhold)

[59] Abeles F 1950 *Ann. Phys.* **5** 596

[60] Gibaud A and Hazra S 2000 *Curr. Sci.* **78** 1467

[61] Kiessig H 1931 *Ann. Phys.* **10** 769–88

[62] Beckmann P and Spizzichino A 1963 *The Scattering of Electromagnetic Waves From Rough Surfaces* (New York: Pergamon)

[63] Névot L and Croce P 1975 *J. Appl. Cryst.* **8** 304

[64] Névot L and Croce P 1980 *Rev. Phys. Appl.* **15** 761–79

[65] Gibaud A 1999 *X-ray and Neutron Reflectivity: Principles and Applications* (Paris: Springer)

[66] Pietsch U, Holy V and Baumbach T 2004 *High-Resolution X-Ray Scattering* (New York: Springer)

[67] Caminiti R and Rossi Albertini V 1999 *Int. Rev. Phys. Chem.* **18** 263

[68] Neissendorfer F, Pietsch U, Brezesinski G and Mohvwald H 1999 *Meas. Sci. Technol.* **10** 354–61

[69] Pietsch U, Grenzer J, Geue Th, Neissendorfer F, Brezesinski G, Symietz Ch, Mohvwald H and Gudat W 2001 *Nucl. Instrum. Methods Phys. Res.* A **467–468** 1077–80

[70] Bodenthin Y, Grenzer J, Lauter R, Pietsch U, Lehmann P, Kurth D G and Mohvwald H 2002 *J. Synchrotron Radiat.* **9** 206–9

[71] Giessen G and Gordon G E 1968 *Science* **159** 973–6

[72] Rossi Albertini V and Paci B 2002 *Rev. Sci. Instrum.* **73** 3160–4

[73] Lee C-H, Yu K-L and Lee H-C 2001 *Nucl. Instrum. Methods Phys. Res.* A **467–468** 1073–6

[74] Windover D, Barnet E, Summers J, Gribbin C, Lu T-M, Kumar A, Bakhru H and Lee S L 2001 *Characterization and Metrology for USLI Technology: 2000 Int. Conf.* (AIP)

[75] Luken E, Ziegler E, Hogoj P, Freund A, Gerdau E and Fontane A 1994 *Physics of Multilayered Structures* (Washington, USA: OSA Technical Digest Series) vol 6

[76] Felici R, Cilloco F, Caminiti R, Sadun C and Rossi Albertini V 1993 *Italian Patent* RM 93 A000410

[77] Windover D, Lu T-M, Lee S L, Kumar A, Bakhru H and Jin C 2000 *Appl. Phys. Lett.* **76** 158–60

[78] Windover D, Barnat E, Lu T-M and Lee S L 2000 *Adv. X-ray Anal.* **42** 590–600

[79] Mahler W, Barberka T A, Pietsch U, Hohne U and Merle H J 1995 *Thin Solid Films* **256** 198–204

[80] Leznoff C C and Lever A B 1989 *Phthalocyanines. Properties and Applications* vol 1–4 (Cambridge, UK: VCH)

[81] Richardson R M and Roser S J 1991 *Langmuir* **7** 1458

[82] Mio Bertolo J, Bearzotti A, Facaro P and Traversa E 2003 *Sensor Lett.* **1** 64–70

[83] Choe G, Chung S J and Walser R M 1995 *Thin Solid films* **259** 231

[84] Chia R W J, Wang C C and Lee J J K 1996 *J. Magn. Magn. Mater.* **155** 146

[85] Jeranko T, Tributsch H, Sariciftci N S and Hummelen J C 2004 *Sol. Energy Mater. Sol. Cells* **83** 247

[86] Wagner C 1933 *Z. Phys. Chem.* B **21** 25

[87] Mott N F 1939 *Trans. Faraday Soc.* **35** 1175

[88] Fromhold A T Jr and Cook E L 1966 *Phys. Rev. Lett* **17** 12112